

# Dynamic Response of Composite Structures in Extreme Loading Environments



Arun Shukla, Christopher Salazar, Shyamal Kishore, and Helio Matos

## 1 Introduction

As the ever-advancing stage of modern warfare threatens civilian and defense structures with extreme loadings under complex conditions [1, 2], the necessity has arisen for new, more blast-resistant structural materials to be researched and understood to ensure the ongoing safety of civilians and military personnel. This has led to the development of composite and sandwich structures, which have important applications in the naval and aerospace industry. Composite materials offer increased strength/weight ratios, energy absorption capabilities, improved corrosion resistance, and low thermal and magnetic signatures. For these reasons, composites are currently used in several military applications, including armored Army vehicles and Navy sonar domes and hull sheathings [3, 4]. However, the principal hindrance to the widespread application of composite and sandwich structures is a lack of complete understanding and simple design rules for their use, especially under extreme loading conditions [4]. For this reason, the current chapter presents the findings of various experimental studies conducted over the past 10 years by researchers at the University of Rhode Island's Dynamic Photo-Mechanics Laboratory which examine the behavior of composite and sandwich structures under extreme in-air and underwater loading environments.

Sandwich structures consist of two thin, stiff facesheets, usually the same thickness, separated by a lightweight, thicker core. The facesheets carry almost all of the bending and in-plane loads, while the core helps to stabilize the facesheets and defines the flexural stiffness and out-of-plane shear and compressive behavior. When sandwich structures are subjected to high-intensity impulse loadings, such as air blasts, the core materials play a crucial role in the dynamic behavior and overall

---

A. Shukla (✉) · C. Salazar · S. Kishore · H. Matos

Department of Mechanical, Industrial and Systems Engineering, University of Rhode Island, Kingston, RI, USA

e-mail: [shuklaa@uri.edu](mailto:shuklaa@uri.edu); [chris\\_salazar@uri.edu](mailto:chris_salazar@uri.edu); [shyamal\\_kishore@uri.edu](mailto:shyamal_kishore@uri.edu)

© Springer Nature Switzerland AG 2020

S. W. Lee (ed.), *Advances in Thick Section Composite and Sandwich Structures*,  
[https://doi.org/10.1007/978-3-030-31065-3\\_1](https://doi.org/10.1007/978-3-030-31065-3_1)

structural response. Their properties assist in dispersing the mechanical impulse that is transmitted into the structure and thus protects anything located behind it [5–7].

In recent years, with its ability to improve structural performance and damage resistance of structures, as well as effectively dissipate blast energy, the application of polyurea to sandwich structures has become a new area of interest. Although the behavior of polyurea has been investigated [8–11], there have been no studies regarding the dynamic behavior of sandwich structures with a functionally graded core and polyurea interlayer. Tekalur et al. [12] experimentally studied the blast resistance and response of polyurea-based layered composite materials subjected to blast loading. Results indicated that sandwich materials prepared by sandwiching the polyurea between two composite skins had the best blast resistance compared to the EVE composite and polyurea layered plates, verifying the material's potential for blast-mitigation.

All underwater loading events presented in this chapter deal with the problem of implosion. An implosion event occurs when a closed, hollow structure of lower internal pressure is submerged in a medium of higher pressure such that the pressure differential results in instability in the structure walls, causing it to collapse inwards on itself. Implosion can also occur below this critical buckling pressure ( $P_c$ ) if the structure is subjected to dynamic deformations exceeding a certain limit [13]. When this occurs underwater, the sudden increase and subsequent arrest in fluid motion emits a pressure pulse into the fluid which can be damaging to and even initiate the implosion of nearby structures [14, 15]. The problem of implosion itself has been a topic of study for many decades, with the first equations for the critical buckling pressure of a hydrostatically loaded cylindrical shell having been derived by von Mises in the early 1900's [16, 17]. The implosion of aluminum tubes has been widely investigated, with Turner and Ambrico having identified the key stages of the implosion process in a free-field environment with respect to the local pressure about the collapsing volume [14]. The harmful effect of these pressure waves on surrounding structures was gained public attention in 2001, at Japan's Super-Kamiokande neutrino observatory, when the implosion of a single photomultiplier tube released a pressure wave powerful enough to trigger a chain reaction of implosion. This accident resulted in the implosion of nearly 7000 nearby tubes, causing \$20–\$30 million in damage [18]. The danger posed to surrounding structures by implodable volumes has thus sparked investigations from researchers in the naval community, with the implosion of composite and sandwich structures at the forefront of most recent investigations.

The experimental investigations detailed in the current chapter are divided into two sections: the response of composite and sandwich structures to air-blast loading and the response of composite and sandwich shells to extreme underwater loadings. In these sections, composite shells, sandwich structures, and structures with the inclusion of polyurea coatings are subjected to extreme loadings, with special attention paid to failure mechanisms and mitigation effects. Note that in the context of air blast loading, mitigation refers to a structure's ability to resist deformation under blast loading. In the context of underwater loading, mitigation refers to a structure's ability to minimize the strength of the pressure pulse resulting from

implosion. In many experimental studies, the capture of high-speed photos coupled with 3D digital image correlation (DIC) is used to quantify the deformation behavior of the structure. Dynamic pressure sensors are used to quantify important pressure data, namely incident and reflected pulses in air blast experiments, and pressures emitted into the surrounding fluid due to UNDEX events, implosion, or both, for underwater experiments. Careful analysis of this data provides key insights into the response of composite and sandwich structures to extreme loading environments, which will aid in the development of optimally designed structures necessary to ensure the ongoing safety of civilians and military personnel.

## **2 Response of Composite and Sandwich Structures to Air-Blast Loading**

This section details various experimental studies conducted to provide insight as to the performance and dynamic behavior of composite and sandwich structures, including those with PU coatings, subject to air blast loading. The section begins by providing a brief description of the physics and operation of the shock tube facility used to create air blast loadings, followed by in-depth theoretical considerations in which the Rankine-Hugoniot relations are utilized to derive expressions which predict reflected pressure during an air blast loading event. The applicability of the expressions to sandwich composite structures is then demonstrated. This section proceeds to detail the effect of foam core gradation in composite sandwich structures and then ends with an overview of two studies conducted to determine the effect of polyurea coatings on the response of composite and sandwich structures to air blast loading. The first of these studies deals with the location of PU coatings on a single composite plate, while the second deals with the location of PU interlayers within composite sandwich structures with sandwich cores.

### ***2.1 Experimental Methods: The Shock Tube Facility***

The shock tube apparatus used to obtain controlled dynamic loading is shown in Fig. 1a. Shock tubes offer the advantages of plane wavefronts, wave parameters that are easily controllable and repeatable, and uniform loading over the shock tube muzzle diameter [19]. A complete description of the shock tube and its calibration is given by LeBlanc et al. [20].

In principle, the shock tube consists of a long rigid cylinder, divided into a high-pressure driver section and a low pressure driven section, which are separated by a diaphragm. By pressurizing the high-pressure driver section, a pressure difference across the diaphragm is created. When this pressure differential reaches a critical value, the diaphragm ruptures. The subsequent rapid release of gas creates a shock

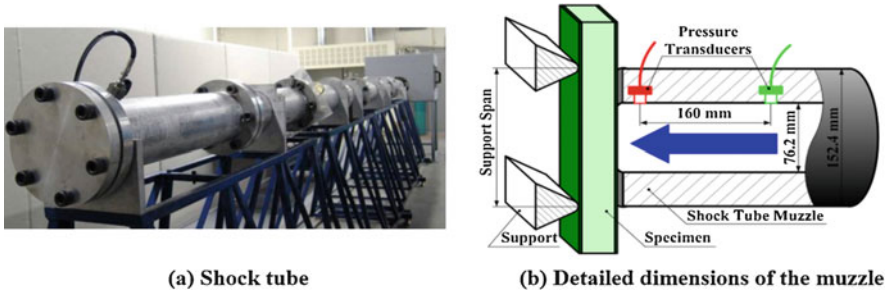


**Fig. 1** Shock tube apparatus

wave, which travels down the shock tube to impart shock loading on the specimen at the muzzle end.

When the shock wave impacts the specimen located at the end of the muzzle, the wave is reflected at a higher pressure than that of the incident shock pressure. The theoretical details on the equations for shock tubes have been previously established in the literature [21]. There are four basic theoretical assumptions which are used to describe the gas flow in shock tube:

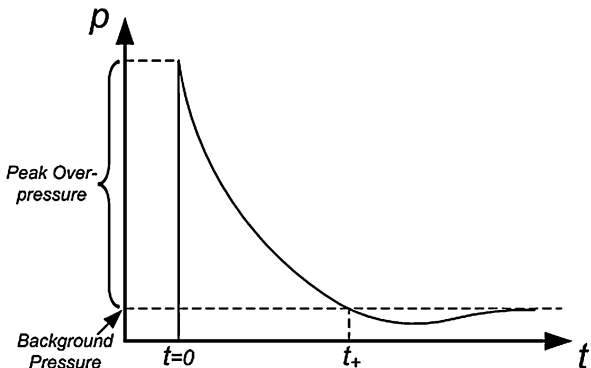
1. The gas flow is one-dimensional.
2. The gas is ideal and has constant specific heats.
3. Heat transfer and viscosity effects are neglected.
4. Diaphragm rupture is instantaneous and does not disturb the subsequent gas flow.

The shock tube apparatus utilized in the present study has an overall length of 8 m, consisting of a driver, driven, converging, and muzzle section. The diameter of the driver and the driven section is 0.15 m. Figure 1b shows detailed dimensions and locations of the muzzle, specimen, supports and the pressure sensors (PCB102A). The sensors are mounted at the end of the muzzle section to measure the incident pressure and the reflected pressure during the experiment. The final muzzle diameter is 0.076 m. The distance between the two sensors is 0.160 m and the distance between the second sensor and the end of the muzzle is  $\sim 0.020$  m.

## 2.2 Theoretical Considerations

In this section, a comprehensive fluid-structure interaction model describing the incident and reflected pressure pulses impinging on a flat structure is presented. Unlike previous models [6, 22–25], this model, derived and validated by Wang et al. [26], considers compressibility of the fluid by utilizing the Rankine-Hugoniot relation of the fluid. The model was then used alongside experimental results to show that the reflected pressure profile can be predicted in sandwich composites by assuming that they are monolithic plates with the same areal density.

**Fig. 2** Typical shock pressure profile



### 2.2.1 Preliminary Considerations

Consider a uniform, planar blast wave propagating with a constant velocity,  $U$ , in a fluid of density  $\rho_f$  and impinging normally upon a free-standing flat target with areal density  $\rho_s$ . An approximate blast pressure profile is shown in Fig. 2. It has a very sharp jump at time  $t = 0$  with a very high overpressure in relation to the background pressure (normally the atmospheric pressure). After the sharp jump, the pressure decays very quickly and even drops to a pressure level lower than the background pressure. The time at which the blast pressure is equal to the background pressure is defined as positive time period,  $t_+$ . The most common approximation of this pulse is expressed with an exponential decay profile [27–29]:

$$p(t) = p_{peak} e^{-\frac{t}{\theta}}, \quad 0 \leq t \leq \infty \quad (1)$$

where,  $p_{peak}$  is the peak pressure.  $\theta$  is the time constant and can be expressed by the positive time period  $t_+$  and the peak pressure  $p_{peak}$ :

$$\theta = \frac{t_+}{\ln(p_{peak}) - \ln(p_0)} \quad (2)$$

where  $p_0$  is the background pressure or base pressure.

Note, for the presented model, the traveling direction of the wave is defined as the positive  $x$  direction,  $x = 0$  is chosen as the original position of the plate, and the out-of-plane displacement of the plate is defined as  $w(t)$ .

### 2.2.2 Model by Wang et al

In the model by Wang et al. [26], compressibility is considered by utilizing the Rankine-Hugoniot relation of the fluid. The incident pressure (represented by the

subscript 1 in Eq. (3a)) and reflected pressure (represented by the subscript 2 in Eq. (3b)) profiles are all assumed to have a similar expression as that of Eq. (1):

$$p_1(t) = p_{1\_peak} e^{-\frac{t}{\theta_1}}, \quad 0 \leq t \leq \infty \quad (3a)$$

$$p_2(t) = p_{2\_peak} e^{-\frac{t}{\theta_2}}, \quad 0 \leq t \leq \infty \quad (3b)$$

where  $p_{1\_peak}$  and  $p_{2\_peak}$  are the peak pressures of the incident and reflected pressure pulses, respectively.  $\theta_1$  and  $\theta_2$  are the time constants for the incident and reflected pressure. Furthermore, assume  $t_{1+}$  and  $t_{2+}$  are the positive time periods for the incident and reflected pressures which can be related to  $\theta_1$  and  $\theta_2$  through Eq. (2).

The reflected pressure profile,  $p_2$ , can thus be calculated from the known incident pressure profile,  $p_1$ , through two steps. The first step is to calculate the peak pressure,  $p_{2\_peak}$ , of the reflected pressure profile by assuming that the incident shock wave is impinging upon a rigid wall:

$$p_{2\_peak} = p_{1\_peak} \left\{ \left[ \frac{u_{1\_peak}}{(1-\mu^2)c_{1\_peak}} + \sqrt{\frac{u_{1\_peak}^2}{(1-\mu^2)^2 c_{1\_peak}^2} + 4} \right]^2 \frac{1+\mu^2}{4} - \mu^2 \right\} \quad (4)$$

where  $u_{1\_peak}$  and  $c_{1\_peak}$  are the peak particle velocity and the peak sound velocity of the incident fluid, respectively. They can be calculated using the incident pressure profile. Note,  $\mu^2 = \frac{\gamma-1}{\gamma+1}$ , where  $\gamma$  is the adiabatic coefficient of the fluid.

The second step is to utilize the conservation of momentum of the plate at the end of the fluid-structure interaction stage:

$$\int_0^{t_+} [p_2(t) - p_0] dt = \rho_s u_2 |_{t=t_+} \quad (5)$$

The reflected target particle velocity,  $u_2$ , can be calculated from the incident and reflected pressure profiles  $p_1$  and  $p_2$ . Since  $p_{2\_peak}$  has been determined in the first step, there is only one unknown parameter in Eq. (5). Therefore, the value of the unknown parameter ( $\theta_2$  or  $t_+$ ) can be obtained by solving Eq. (5). Consequently, all of the parameters, such as impulse, can be generated using the calculated reflected pressure profile,  $p_2$ , and the known incident pressure profile  $p_1$ . Further details regarding the steps and generation of parameters can be found in [26].

### 2.2.3 Application of the Model by Wang et al. to Sandwich Composite Structures of Varying Areal Density

The fluid-structure interaction model derived in the previous sections of Sect. 2.2 was developed by Wang et al. and thus will be referred to as the Wang model. Other models have been previously derived to describe the magnitude of reflected pressure resulting from shock loading generated by a shock tube, namely the Taylor model [23] and the Kambouchev model [24, 25]. These models, however, do not consider the compressibility of gas that the Wang model considers, and thus result in a large deviation from experimental results for shock loading in air [30]. To demonstrate the applicability of the Wang model to air blast loading scenarios, a series of experiments were conducted in which composite structures and a monolithic Al plate under simply supported conditions were subjected to air blast loading in air, and the reflected pressure profiles compared to values predicted using the Wang model.

The structures subjected to blast loading were an EVE composite plate, a sandwich composite with 25.4 mm monolithic foam core, a sandwich composite with 38.1 mm monolithic foam core, and a monolithic Al alloy 6061-T6 plate. The weight and areal density of the structures used are found in Table 1. The shock tube facility discussed in Sect. 2.1 was used to provide the air blast loading with a peak incident pressure of 1 MPa. Further experimental details can be found in [30].

The predicted reflected pressure profiles, as obtained using Taylor's model and the Wang model are shown in Fig. 3. Since the two models can only predict the behavior of a free-standing specimen, the simply-supported boundary conditions are completely ignored in the calculation. Therefore, the results are only valid during the characteristic fluid-structure interaction time, in which the simply supported boundary conditions have not affected the dynamic behaviors of the structure. The results in Fig. 3 validate the above assumption. It can be seen clearly that during the characteristic fluid-structure interaction time ( $\sim 250 \mu\text{s}$ ), the predictions from the Wang model agrees well with experimental results. The predictions even agree with the experimental results through  $t = 500 \mu\text{s}$ . After this time, the predictions drift off the experimental data, which shows the boundary condition effects on the results. Unlike the Wang model, the Taylor model does not consider the compressibility of the gas and thus the theoretical predictions exhibit a large deviation from the experimental results. This reveals that the Taylor model cannot be used in a highly compressible fluid such as air.

**Table 1** Weight and areal density of shock-loaded structures

Specimen name	Weight (g)	Areal density ( $\text{kg/m}^3$ )
EVE composite	177	6.8
Sandwich composite with 25.4 mm foam core	446	17.2
Sandwich composite with 38.1 mm foam core	600	23.3
Al alloy 6061-T6	660	25.7

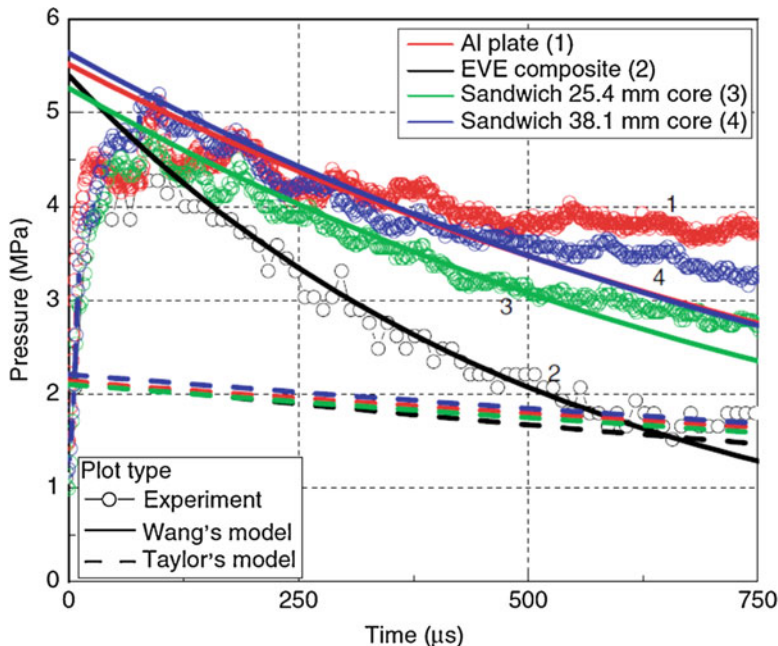


**Fig. 3** Comparison of theoretical and experimental reflected pressure profiles

It has been assumed in previous studies [6, 22] that when a sandwich composite structure is subject to blast loading, fluid-structure interaction only occurs between the fluid and the facesheet of the structure. That is, it was assumed that core material and core thickness do not play a role. Numerical studies [31] have shown that the fluid-structure interaction is indeed affected by the core material. The results obtained by Wang et al. provide a much clearer and more comprehensive understanding of the fluid-structure interaction in sandwich composites. The experimental results and theoretical predictions of the sandwich composites and the facesheets (EVE composites) are plotted in Fig. 3. For the theoretical prediction, the sandwich composite is considered to be an equivalent monolithic plate. It can be clearly seen that the fluid-structure interaction between the fluid and the sandwich composites is completely different than that between the fluid and the EVE facesheet. Using the prediction of the facesheet will induce significant error. Furthermore, sandwich composites which have a core of identical material but different thicknesses exhibit different responses from the very beginning. This indicates that the core material affects the fluid-structure interaction. These results indicate that using the Wang model and assuming the sandwich composite to be an equivalent monolithic plate with same areal density allows for a close prediction of the reflected pressure profiles during the characteristic fluid-structure interaction time.



## 2.3 Air Blast Response of Composite Sandwich Structures

### 2.3.1 Effect of Functional Foam Core Gradation

This section details a series of experiments conducted by Gardner et al. [32] which consisted of subjecting simply supported composite sandwich structures of various core gradation configurations to air blast loading with 1 MPa incident pressure and 5 MPa reflected pressure. The shock tube apparatus used to generate air blast loading is detailed in Sect. 2.1 of this chapter, and the sandwich structures being loaded were fabricated in the configurations given by Table 2.

All sandwich structures were fabricated using the Vacuum Assisted Resin Transfer Molding (VARTM) process with 4 mm thick EVE facesheets, and were 254 mm long with a width of 102 mm. Note that areal densities for all configurations are very similar. Finally, it should be noted that the core materials, read from left to right, indicate the gradation sequence, with the leftmost core adjacent to the front (loaded) faceplate, and the rightmost core adjacent to the back faceplate. Properties of the materials used can be found in [33, 34].

In a study conducted by Wang et al. [35], it was shown that sandwich structures with graded foam cores of increasing nominal density showed least back-face deflection, as this allowed for more core compression. That is, sandwich structures with graded cores arranged with the softest nearest the shock and the hardest furthest from the shock resulted in more effective mitigation. Thus, the sequence of the foam core material for this study was designed based on increasing the one-dimensional acoustic wave impedance of the layers. That is, for the A-series foam, the A300 foam has the lowest nominal density ( $\rho$ ) and compressive modulus ( $E$ ) of the four foams, followed by the A400, A500, and A800 foams respectively. Since both the nominal density and the compressive modulus are increasing from the A300 foam to the A800 foam, the one-dimensional acoustic wave impedance ( $Z$ ) is also increasing, and shows the following relationship:

$$Z = \rho C = \rho \sqrt{E/\rho} \quad (6)$$

$$Z_{A300} < Z_{400} < Z_{A500} < Z_{A800} \quad (7)$$

Note, the cell structures of the four A-series foams are very similar and the only difference appears in the cell wall thickness and node sizes, which accounts for the

**Table 2** Material system configurations for sandwich structures with functionally graded foam cores

Core materials	Core thickness	Areal density (kg/m <sup>3</sup> )
A500	38 mm	19.0
A300, A800	19 mm each	18.5
A300, A500, A800	12.7 mm each	19.0
A300, A400, A500, A800	9.5 mm each	20.0

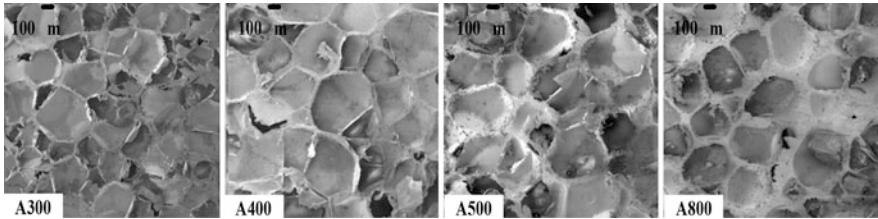


**Fig. 4** Cell microstructure of A-series foam core layers

different densities of the foams. The SEM images of the cell microstructures can be seen in Fig. 4.

It was shown that the number of core layers has an influence on the dynamic response of structures under blast loading. More specifically, by increasing the number of monotonically graded layers, the acoustic wave impedance mismatch between successive layers is reduced. Therefore, the strength of the initial shock wave (stress wave) can be weakened by the time it reaches the back facesheet, resulting in lower back face deflection, in-plane strain, and velocity. More importantly, the overall damage imparted on the structure can be reduced and structural integrity can be maintained. Also, increasing the number of monotonically graded foam core layers, thus introducing more material interfaces, allows for blast wave (stress wave) attenuation through the following mechanisms: (1) stepwise compression of the core (energy dissipation mechanism) and (2) scattering/dispersion of the wave through interface variations. Combining these mechanisms results in lengthened timescales for pressure rises across the samples, allowing for a time-delay of the peak stress arrival, and thus delaying the time of damage initiation. The following sections elucidate the effects a functionally graded styrene acrylonitrile (SAN) foam core on the blast response of sandwich composites.

### 2.3.1.1 Deflection

The mid-point deflections of each graded sandwich panel and all of its constituents were obtained from the high-speed images and a typical response can be seen in Fig. 5. The difference between the deflection of the front face and deflection of the back face signifies the total amount of compression observed in the core.

It should be noted that for all of the configurations studied, the core layers were graded monotonically by increasing the acoustic wave impedance, therefore allowing for a stepwise compression of the core. This stepwise compression is more evident in the three and four-layer core configurations, i.e. Fig. 5c and 5d.

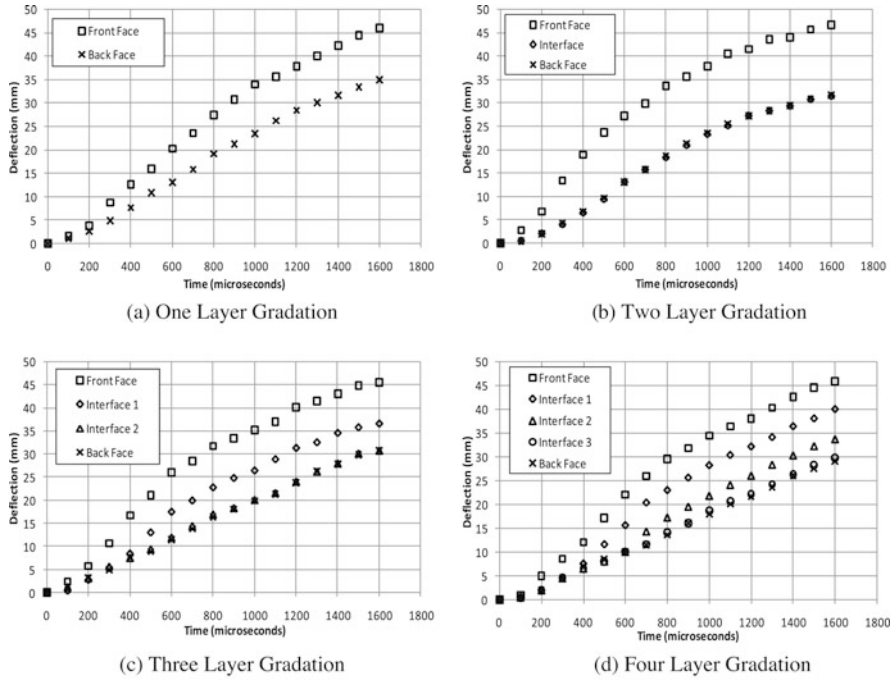
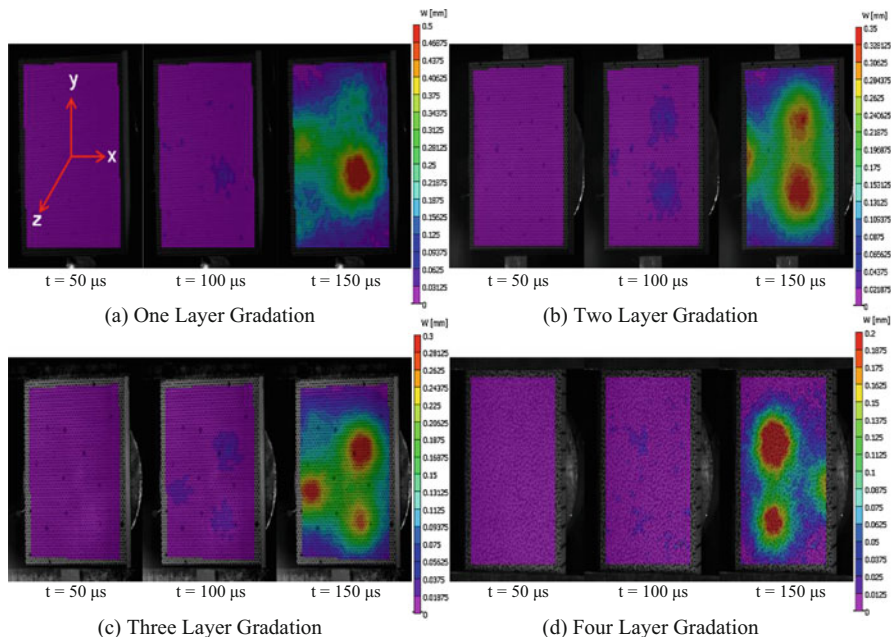


Fig. 5 Mid-point deflection of all configurations

2.3.1.2 DIC Analysis

Utilizing the DIC technique, the full-field deflection, in-plane strain and particle velocity of the back facesheet of each configuration were generated. Figures 6a, 6b, 6c and 6d, show the full-field results for the back facesheet of all core gradations respectively. Figure 6 shows the full-field out-of-plane deflection (W) during the initial fluid-structure interaction ( $t \leq 250 \mu s$ ), with an emphasis on the shape of the loading, as indicated by the localized areas of larger deflection. Note that the scale used to represent each core gradation is different in order to highlight these areas. For one-layer core gradation, as shown in Fig. 6a, by  $\sim t = 150 \mu s$ , the loading can be observed as a circular region in the center of the back facesheet. For two, three and four-layer core gradation, as shown in Figs. 6b, 6c, and 6d respectively, by  $t = 150 \mu s$  the loading is more dispersed across the back facesheet, resulting in two and even three areas of localized deflection (loading). Therefore, it can be concluded that utilizing multiple layers of core gradation, and thus introducing more material interfaces, aids in dispersing the initial loading on the structure, resulting in up to three areas of localized deflection (loading) on the back facesheets.

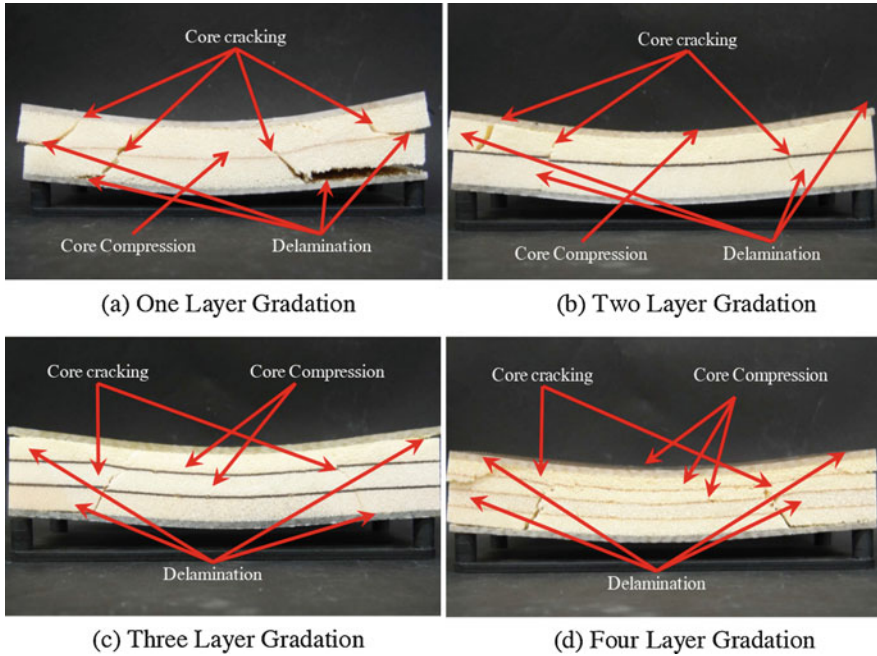


**Fig. 6** Localized areas of larger deflections (loading) during fluid-structure interaction

### 2.3.1.3 Damage Mechanisms

After the blast loading event occurred, the damage patterns of the sandwich composites with four different core layer arrangements were visually examined and recorded using a high-resolution digital camera and are shown in Fig. 7. When the sandwich composite with one-layer core gradation was subjected to highly-transient loading, as shown in Fig. 7a, the damage was confined to the areas where the supports were located in the shock tube and core cracking is visible in these two areas. The core cracks propagated completely through the foam core. Core delamination is visible between the two core layers of A500 foam. Some core compression is also visible in the first core layer of A500 foam.

For the sandwich composite with two layers of core gradation, the damage patterns after being subjected to the shock loading are shown in Fig. 7b. For this core configuration, the damage was again confined to the areas where the supports were located in the shock tube and core cracking is evident. The core cracks propagated completely through the foam core. Skin delamination is obvious between the front facesheet and the foam core, as well as back skin delamination between the back facesheet and the foam core. Core delamination between the first and second core layers of foam, A300, and A800 respectively, is also evident, along with core compression in the first core layer of foam (A300).



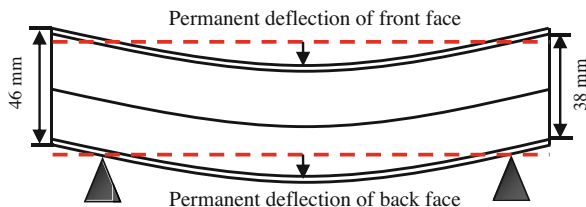
**Fig. 7** Post-mortem examination of all core configurations

Figure 7c shows the damage patterns of the sandwich composite with three layers of core gradation after the blast loading event occurred. Again, the damage to this core configuration was confined to the areas where the supports were located in the shock tube and core cracking is visible in these two areas. These core cracks propagated completely through the foam core. Also, skin delamination is visible between the front facesheet and the foam core, as well as back skin delamination located between the back facesheet and the foam core. Core compression is also evident in both the first and second core layers of foam, A300, and A500 respectively.

When the sandwich composite with four layers of core gradation was subjected to the shock loading, as shown in Fig. 7d, the damage was again confined to the areas where the supports from the shock tube were located and core cracking is evident in these two areas. Unlike the previous three configurations, the core cracks did not propagate completely through the foam core. Core delamination is obvious between the first and second core layers of foam, A300, and A400, as well as back skin delamination between the back facesheet and the foam core. Core compression is very obvious in this configuration. The first, second and third layers of foam, A300, A400, and A500 respectively, all exhibit various amounts of core compression.

The permanent deflection (deformation) for each graded core configuration was measured after the shock loading experiment. A schematic of the specimen and how the measurements were taken can be seen in Fig. 8. The distance between the top

**Fig. 8** Specimen schematic for permanent deflection measurements (between simple-supports)



**Table 3** Permanent deflection and core compression

	1 Layer	2 Layer	3 Layer	4 Layer
Permanent front face deflection (mm)	11.1	14.1	12.9	12.4
Permanent back face deflection (mm)	8.5	9.2	7.3	6.1
Final core thickness (mm)	35.4	33.1	32.4	31.7
Permanent core compression (mm/%)	2.6 (7%)	4.9 (13%)	5.6 (15%)	6.3 (17%)
Real-time core compression (mm/%)	11 (30%)	13 (35%)	15 (40%)	17 (45%)
Recovered (mm/%)	8.4 (23%)	8.1 (22%)	9.4 (25%)	10.7 (28%)

dotted line (red) and the surface of the front facesheet is defined as the permanent deflection of the front face. Similarly, the distance between the bottom dotted line and the top surface of the back facesheet is defined as the permanent deflection of the back face. Subtracting the total permanent deflection of the back face from the front face, the final core thickness and thus total core compression (permanent) can be obtained. These values are shown in Table 3.

## 2.4 Air Blast Response of Composite Structures With Polyurea Coatings

With its ability to improve structural performance and damage resistance of structures, as well as effectively dissipate blast energy, the application of polyurea to composite structures has become a new area of interest. The following sections reveal the importance of polyurea and the effect of its location on the blast response of composite plate and sandwich structures.

### 2.4.1 Effect of Polyurea on Composite Plates

To determine the deformation and damage mechanisms at play in the air blast loading of EVE composite panels with PU coatings, a series of shock tube experiments were conducted which varied the location of PU on EVE composite panels [12]. Results were compared against plain-woven composite panels without PU coating. The shock tube shown in Fig. 1 was used to provide the loading on simply supported specimens, and their response was recorded using the high-speed digital

imaging system detailed in [12]. The panels of plain-woven composite were 6 mm (0.25") nominal thickness and panels of layered composite were 12 mm (0.5") nominal thickness that includes 6 mm (0.25") of plain-woven composite and 6 mm (0.25") of polyurea coating. The layered composites were tested in two different ways, namely:

1. PU side facing the shock blast (henceforth referred to as PU/EVE)
2. EVE side facing the shock blast (henceforth referred to as EVE/PU)

For EVE plates subjected to simply supported boundary conditions, the lamina facing the oncoming shock front is largely subjected to compression, while the lamina on the back of the plate is largely in tension. This is important because, in EVE composite plates, the tensile strength is much greater than the compressive strength as tensile strength is dominated by the fibers and compressive strength is dominated by the vinyl-ester matrix. Due to this fact, it was found in this study that PU/EVE plates responded much better to air blast loading than EVE/PU plates. This is because when polyurea is applied to the composite lamina that largely undergoes compression, the increase in compressive strength is large compared to that of the composite. When applied to the back face, however, the additional strengthening is relatively little. This fact plays a large role in the center point deflections and damage mechanisms of EVE plates subjected to air blast loading.

### 2.4.1.1 Center Point Deflection

The center point deflection of the plate was calculated from the high-speed images and normalized to unit thickness to provide a good comparison of structure response. Figure 9 provides a normalized plot of deflections per unit thickness of the plain composite and layered materials under the same or comparable input blast loadings. Also shown in Fig. 9 are the deformed EVE, PU/EVE, and EVE/PU specimens showing clear variations in damage. The input pressure is stated in the legend for each material. These plots reveal that the deflections observed in the layered constructions were lower than those observed in the plain composite plates, as

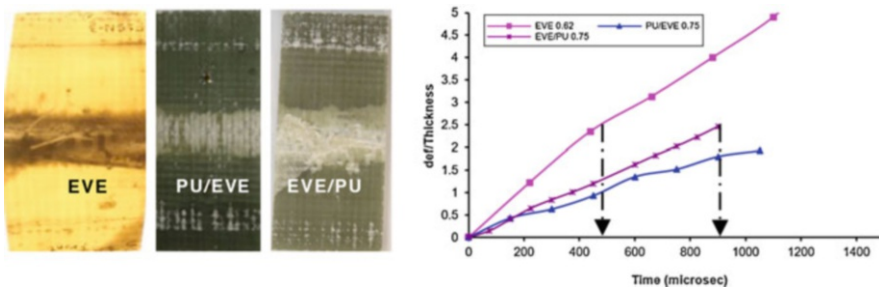


**Fig. 9** Damaged EVE, PU/EVE, and EVE/PU structures shown alongside respective deformation plots normalized to unit thickness, under comparable input blast loading



expected. The quantitative estimate of the reduction in deflections can be observed from these plots. Also to be noted is that the input blast pressure is much lower for the plain composite compared to the layered constructions.

In case of the plain composite materials, the “failure” point (deflections equaling 2.5 times the thickness) is produced at an earlier time compared to the layered system under comparable input blast loadings. Also, in the case of polyurea facing the blast, the failure point is not observed at all. The macroscopic damage in the plate also corroborates with the observed real-time trend, vis-à-vis, the PU/EVE configuration showing lower damage area compared to the EVE/PU configuration.

Under the same input blast loadings, the sandwich configuration showed normalized deflections less than one, which is well within the elastic limits of the plate. Here again, it was observed that the PU/EVE configuration reached the failure point at a later time stage compared to the EVE/PU configuration. The delay in the attainment of this failure point between the layered configurations can be attributed to the internal strengthening mechanisms that are present in the PU/EVE system.

#### 2.4.1.2 Failure Mechanisms

Microscopic analysis of undamaged and damaged specimens was conducted using a Nikon SMZ Microscope to provide insight as to the impact of polyurea on damage in the structure. This analysis was conducted for EVE, PU/EVE, and EVE/PU configurations. Detailed microscopic used for this analysis are given by Tekalur et al. [12].

##### (a) EVE composite

The damage modes observed in blast loaded plain-woven composite included fiber breakage and interface failure. The tensile properties of these composites are superior to the compressive properties. This explains the initiation and the mode of damage on the impact side, which is predominantly under compression. Crushing and cleavage of the longitudinal fiber are observed in these panels. The straight cleavage of a longitudinal fiber bundle near the midsection observed in suggests that the fiber bundle had been crushed compressively during the initial phase of loading and subsequently pulled in tension due to the reflection of the waves from the rear surface, leading to an interface failure between the longitudinal and transverse fiber regions.

##### (b) PU/EVE layered structure

Addition of a PU layer provides additional modes of damage and hence added energy dissipation mechanisms. In addition to the interface between the transverse and longitudinal fiber directions, the layered materials also have a PU interface with these directions. When studied under the microscope, the predominant damage modes observed in PU/EVE layered materials were:

1. Fiber direction tensile failure
2. Matrix direction failure (observed as voids created through tensile separation)



### 3. PU-EVE Interface failure (with both the directions)

As noted, the damage modes observed in PU/EVE were predominantly tensile failure patterns. It is also observed that the bonding between the Polyurea and the transverse layer is weaker than the bonding between Polyurea and longitudinal fiber directions when a layered composite plate is subjected to blast.

#### (c) EVE/PU layered composite

When the loading direction was reversed (i.e., EVE on the impact side), compression dominated failure mode (fiber crushing) was observed. Again, the interface between polyurea and the transverse fiber direction was observed to be weaker than the interface between polyurea and longitudinal direction. In these layered materials, the microscopic failure mode was dominated by compressive failure patterns like crushing of the transverse and longitudinal fibers. The macroscopic failure patterns also correspond to compressive and shear failure on the strike face of composite plates.

The strengthening or the enhanced blast performance in the layered composite can be attributed to the following factors:

1. Energy dissipation due to the nonlinear and highly rate dependent properties of the polyurea layer
2. Energy dissipation in the failure of polyurea-composite interfaces.

However, the explanation for the observance of better performance of a specific orientation (PU/EVE) needs a thorough understanding. It was seen during dynamic material characterization [12] that when the loading is uni-axial, the stress response is not significantly different whether the polyurea faces the impact or composite faces the impact. But, in case of blast loading of a layered plate, wherein the loading induces multi-dimensional stress fields, an additional strengthening mechanism is involved. When polyurea is on the strike face, the composite lamina that is in direct contact with the polyurea is provided with strengthening against compressive and shear failure. So the damage initiation in this lamina will require additional energy from the blast. This will not be true when the composite lamina faces the initial blast directly. The impact face, wherein the first lamina is exposed to a severe compressive zone, begins to fail and thus, the overall strength of the structure reduces progressively as the blast loading progresses. Since the reinforcement of polyurea was on the tensile zone and not the compressive zone, the enhancement in blast performance of these layered composites was comparatively lower than when the polyurea faced the blast loading.

#### **2.4.2 Effect of Polyurea Location Within Composite Sandwich Structures**

Thus far, Sects. 2.3.1 and 2.4.1 have discussed the effect of foam core gradation in sandwich structures and the effect of PU coatings on EVE plates, respectively.

**Table 4** Material system configurations for sandwich structures with graded foam cores and PU interlayer

Core materials	Core thickness (mm)	Areal density
PU, A300, A500, A800	6.35, 12.7, 12.7, 6.35	26.0
A300, A500, A800, PU	12.7, 12.7, 6.35, 6.35	26.0

However, the question remains as to the effect of PU interlayers within sandwich structures with graded foam cores. To address this question, this section presents the results of a series of air blast experiments conducted by Gardner et al. [36] on A300/A500/A800 graded sandwich structures (identical to those of Figs. 5c, 6c, and 7c, of Sect. 2.3.1) with the inclusion of a PU interlayer. The air blast loading with peak incident and reflective pressures of 1 MPa and 5 MPa respectively was produced using the shock tube apparatus discussed in Sect. 2.1. Graded sandwich structures with PU interlayers were simply supported and fabricated using the VARTM process in the configurations shown in Table 4.

All sandwich structures were fabricated with 4 mm thick EVE facesheets, and were 254 mm long with a width of 102 mm. It should be noted that the core materials, read from left to right, indicate the gradation sequence, with the leftmost material adjacent to the front (loaded) faceplate, and the rightmost material adjacent to the back faceplate. Dragonshield-HT polyurea was used as the PU interlayer. Properties of the materials, including EVE facesheet used, can be found in [33, 34, 37].

When the polyurea interlayer is located behind the graded foam core (configuration 1), and in front of the back face (configuration 2), the core layer arrangement allows for a stepwise compression of the core. Larger compression was visible in the A300 and A500 foam core layers of configuration 2 than configuration 1. This compression lowers the strength of the initial shock wave by the time it reaches the back facesheet and thus the overall deflection, in-plane strain, and velocity were reduced in comparison to the sandwich composite with the polyurea interlayer located behind the front facesheet and in front of the foam core (configuration 1). Therefore, it can be concluded that placing the polyurea interlayer behind the foam core and in front of the back facesheet (configuration 2) improves the blast resistance of the sandwich composite and better maintains structural integrity. It was observed that the location of the polyurea layer has a significant positive effect on the response of composite sandwich panels to shock wave loading, both in terms of failure mitigation and energy absorption, if it is placed opposite the blast-receiving side (configuration 2). On the contrary, the presence of polyurea on the blast-receiving side (configuration 1), amplifies the destructive effect of the blast, promoting (rather than mitigating) the failure of the composite sandwich panels. The following sections detail the experimental results of subjecting functionally graded sandwich structures with PU interlayers to blast loading.

2.4.2.1 Interface Deflection

The mid-point deflections of the constituents of sandwich composites with different core configuration were obtained from the high-speed side-view images and shown in Fig. 10. For configuration 1, the mid-point deflection of the front face (front skin), interface 1 (between first and second core layer), interface 2 (between second and third core layer), interface 3 (between third and fourth core layer), and back face (back skin) were plotted and are shown in Fig. 10a. Since the front face and interface 1 deflect in the same manner to the same value (43 mm), it signifies that the polyurea interlayer, which is located between the front face and interface 1, exhibits no compression. Since interface 2, interface 3, and the back face all deflected in a similar manner to the same value of approximately 34 mm, it can be concluded that the A500 foam layer (located between interface 2 and interface 3) and the A800 foam layer (located between interface 3 and the back face) showed no compression. Therefore, the core layer arrangement of configuration 1 allows for compression only in the A300 layer of foam and has a front face and back face deflection of approximately 43 mm and 34 mm respectively.

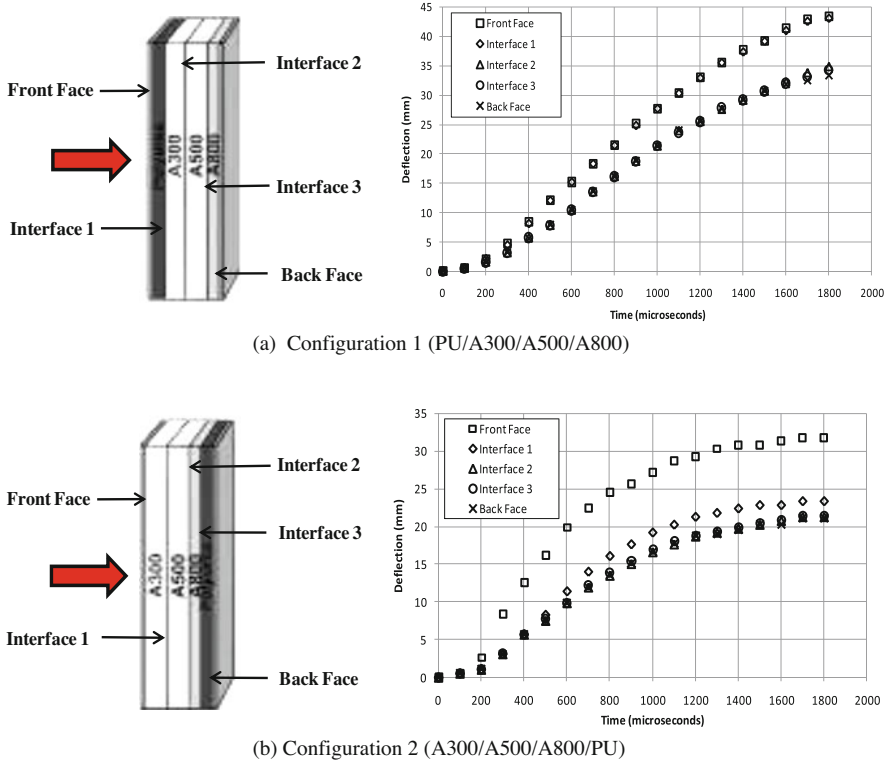


Fig. 10 Mid-point deflection of both configurations

For configuration 2, the mid-point deflection of the front face (front skin), interface 1 (between first and second core layer), interface 2 (between second and third core layer), interface 3 (between third and fourth core layer), and back face (back skin) were plotted and are shown in Fig. 10b. It should be noted that interface 2, interface 3 and the back face all deflected in a similar manner to the same value of approximately 21 mm, and thus there was no compression in the third and fourth core layer (A500 foam layer and the polyurea interlayer). Therefore, the core arrangement of configuration 2 allows for a stepwise compression through the core and the front face and back face deflect to approximately 33 mm and 21 mm respectively.

#### 2.4.2.2 DIC Analysis

Utilizing the DIC technique, the in-plane deflection contours of the back facesheet for each configuration were generated. Figure. 11 shows the full-field out-of-plane deflection ( $W$ ) with a scale of 0 mm (purple) to 32 mm (red). It is evident from the figure that for configuration 1, the back face exhibits very little out-of-plane deflection until approximately  $t = 400 \mu\text{s}$ . Between  $t = 400 \mu\text{s}$  and  $t = 1800 \mu\text{s}$ , the panel continues to show deflection.

By  $t = 1800 \mu\text{s}$ , it can be observed that the central region of the panel has deflected approximately 32 mm. For configuration 2, as shown in Fig. 11b, the back

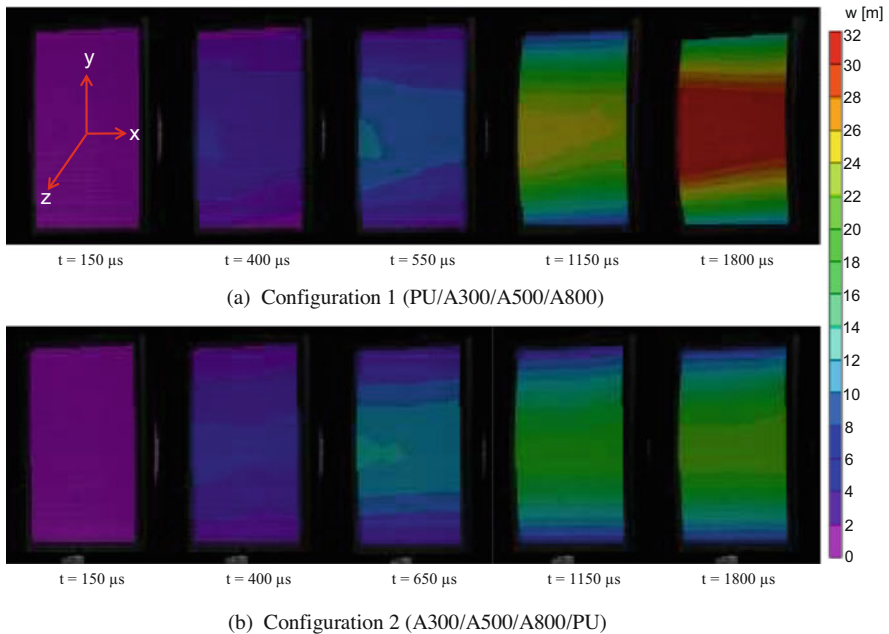


**Fig. 11** Full-field out-of-plane deflection ( $W$ ) of both configurations

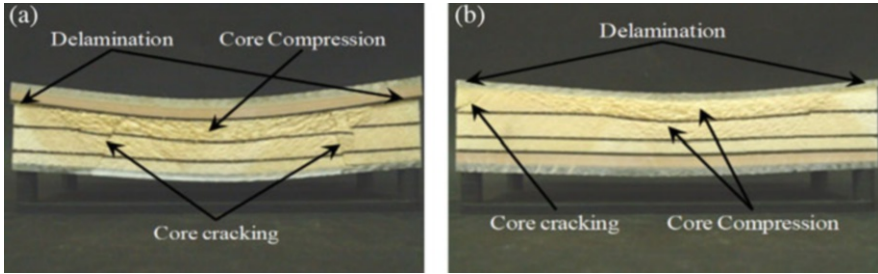


**Fig. 12** Post-mortem examination of (a) configuration 1 and (b) configuration 2

face shows very little out-of-plane deflection until  $t = 400 \mu\text{s}$ . Between  $t = 400 \mu\text{s}$  and  $t = 1800 \mu\text{s}$ , the panel continues to exhibit deflection. By  $t = 1800 \mu\text{s}$ , the central region of the panel has deflected approximately 22 mm. Therefore, configuration 2 deflects approximately 35% less than configuration 1.

#### 2.4.2.3 Failure Mechanisms

After the blast loading event occurred, the damage patterns of both configuration 1 and configuration 2 were visually examined and recorded using a high-resolution digital camera and are shown in Fig. 12. When configuration 1 was subjected to transient shock wave loading, as shown in Fig. 12a, the damage was confined to the areas where the supports were located in the shock tube and core cracking is visible in these two areas. The core cracks propagated completely through the foam core to the polyurea interlayer. Core delamination is visible between the polyurea interlayer, and the first layer of the foam core (A300). Core compression is visible in the first core layer of A300 foam.

When configuration 2 was subjected to transient shock wave loading, the damage patterns can be seen in Fig. 12b. For this configuration, very little core damage was observed. Core delamination between the first two layers of the foam core (A300 and A500) led to a crack that propagated through the first foam core layer (A300) to the front facesheet. Skin delamination was evident between the front face and the first foam core layer (A300). Also core compression can be observed in the first two layers of the foam core (A300 and A500).

### 3 Response of Composite and Sandwich Structures to Extreme Underwater Loading Environments

The studies presented in this section cover the advances in the underwater implosion of both thin and sandwich composite shell structures. In Sects. 3.2 and 3.5 the mechanics of the hydrostatic and shock initiated collapse, as well as the emitted

pressure pulses released, are characterized for the two structures respectively in free-field. Finally, Sect. 3.3 mitigation explores strategies to reduce the strength of the implosion pulse resulting from the collapse of thin shell composites.

### 3.1 Experimental Methods: Free-Field Implosion

To simulate free-field conditions experiments were conducted in a large spherical (2.1 m dia.) pressure vessel with a maximum pressure rating of 6.89 MPa to provide constant hydrostatic pressure throughout the collapse event (Fig. 13). Several high-pressure windows mounted about the midspan of the vessel allow the specimens to be viewed by high-speed cameras (Photron SA1, Photron USA, Inc.), and adequately lit by high-intensity light sources. The specimens were securely suspended horizontally in the center of the pressure vessel using several steel cables attached to the inner walls of the vessel. To measure the changes in local pressure during the collapse event, several dynamic pressure transducers (PCB 138A05, PCB Piezotronics, Inc., Depew, NY) were mounted at different locations about the specimens either axially or circumferentially or both depending on the study. A few locations of pressure sensors with a standoff distance  $R_s$  are illustrated in Fig. 13 for illustration. The vessel is then flooded with filtered water for maximum optical clarity, leaving a small air pocket at the top. Once the vessel is filled, nitrogen gas is introduced into the air pocket to pressurize the vessel. The pressure inside the vessel is increased at a gradual rate (0.083 MPa/min) until the specimen collapsed triggering the cameras and the pressure sensors to record data. 3-D Digital image correlation (DIC) a well-known experimental tool is used to determine real-time, full-field displacements across the viewable surface of the specimen throughout the implosion event [38]. This technique is calibrated for underwater testing based on previous work [39] for good confidence in the accuracy of measured displacements and

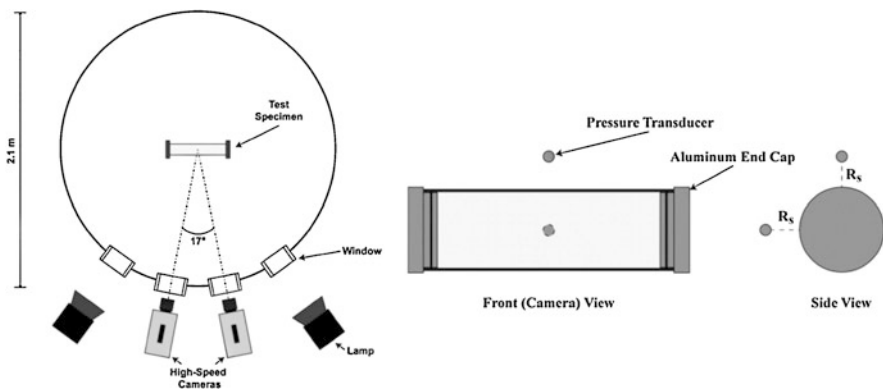


Fig. 13 Experimental apparatus to simulate free-field conditions

velocities. A generalized description of this pressure chamber facility is given by Gupta et al. [39], however, specific details of experimental setups of the studies discussed in this chapter are given in those studies' respective published journal articles.

## **3.2 *Hydrostatic and Shock Initiated Implosion of Thin Cylindrical Composite Shells in Free-Field Environment***

A review of free-field implosion related investigations of thin cylindrical composite shells are presented in several following subsections:

1. In Sect. 3.2.1 an experimental study of the hydrostatic implosion of carbon fiber reinforced epoxy composite tubes to examine the failure and damage mechanisms of collapse is presented.
2. In Sect. 3.2.2 the mechanisms and pressure fields associated with the hydrostatic implosion of glass-fiber reinforced polymer (GFRP) tubes with varying reinforcement are presented.
3. In Sect. 3.2.3 a comprehensive investigation of the implosion of thin composite cylinders subjected to a nearby explosion is presented.

### **3.2.1 Hydrostatic Implosion of Thin Cylindrical Carbon Composite Shells**

This section details experiments conducted by Pinto et al. [40] on the hydrostatic implosion of carbon fiber reinforced epoxy composite tubes to examine the failure and damage mechanisms of collapse. Experiments were performed in the pressure vessel shown in Sect. 3.1. The implodable volumes used in this study were laminated carbon/epoxy composite tubes. Three different reinforcing fabric architectures are studied: filament-wound, roll-wrapped, and braided carbon fabric. The filament-wound tubes consist of seven layers of unidirectional carbon fabric reinforcement arranged in a  $[\pm 15/90/\pm 45/\pm 15]$  layup. Tubes of two different inner diameters were studied, 76.2 mm (notated as CT) and 60.3 mm (notated as CTRD). The roll-wrapped tubes contain 11 layers of unidirectional tape, arranged in a  $[0_3/\pm 45/90/\pm 45/0_3]$  layup. The braided composite tubes were constructed of two layers of braided carbon fabric reinforcement sandwiching one unidirectional layer to obtain a  $[\pm 45/90/\pm 45]$  layup. Table 5 gives the details of the specimens used in this study. The dimensions were selected to provide specimens with a relatively low expected collapse pressure, and a high radius-to-thickness ratio ( $>18$ ) so that thin-wall assumptions may be utilized. It was found that the quantitative characteristics of the released pressure pulse during the implosion of the specimens as well as the nature of their collapse itself are significantly affected by the architecture of reinforcing fibers and geometry of the tube. In particular, the composites with

**Table 5** Geometric and material properties of studied specimens

Specimen	Reinforcement	Inner diameter (mm)	Wall thickness (mm)	L/D	Effective modulus (GPa)	Collapse pressure, $P_{cr}$ (MPa)
CT	Filament-wound	76.4	1.39	3.7	74.2	0.73[±0.01]
CTRD	Filament-wound	60.4	1.58	4.6	78.4	1.61[±0.09]
RC	Roll-wrapped	76.3	1.63	3.7	91.1	0.75[±0.06]
BC	Braided	75.8	2.12	3.7	41.0	1.83[±0.10]

braided fabric reinforcements have more damage potential to adjacent structures than those containing unidirectional reinforcements, as they release pressure waves with significantly greater impulse. The results of this study have been succinctly discussed in the following subsections.

### 3.2.1.1 Deformation and Post-buckling Analysis

The deformation and the post-buckling response of the different specimens are compared and contrasted below. For the sake of brevity, only the first case will be examined in detail and the other cases will be discussed highlighting the differences to previous cases.

#### (a) Large Diameter Filament-Wound Specimens (CT)

The larger diameter CT specimens failed violently at approximately 0.73 MPa. These tubes buckled in a mode 3 shape, collapsing completely during the failure process then rebounding to a roughly cylindrical shape following the release of pressure. The averaged local dynamic pressure trace about the midspan of the specimen at a standoff distance of 48.3 mm is shown in Fig. 14, and high-speed images, as well as DIC, generated displacement and velocity contours corresponding to key points on the trace are seen in Fig. 15.

Before the start of the rapid and unstable collapse of the structure, a significant amount of slow, quasi-static deformation is measured by DIC. For CT tubes, this initial ovaling amounts to  $-4.31$  mm (11% of the tube radius), a very significant amount of deformation which may serve as an early warning of implosion risk. As the collapse initiates, the local pressure about the midspan decays somewhat smoothly for about 4.5 ms, from time A to time B. By examining the correlated images for this period, it is seen that this pressure decays corresponding with the buckling of the tube in a mode 3 shape, without visible damage. At time B, a longitudinal crack is observed on the bottom visible lobe of the structure, pursued immediately by a small amount of cavitation on that surface. This is followed by an abrupt drop in local pressure, caused by the increased acceleration due to the loss of structural stability in that region brought on by cracking. The local pressure continues to fall until it reaches a minimum at time C. At this instant, it is observed that surface cavitation has intensified, reflecting this drop in pressure. A sudden increase



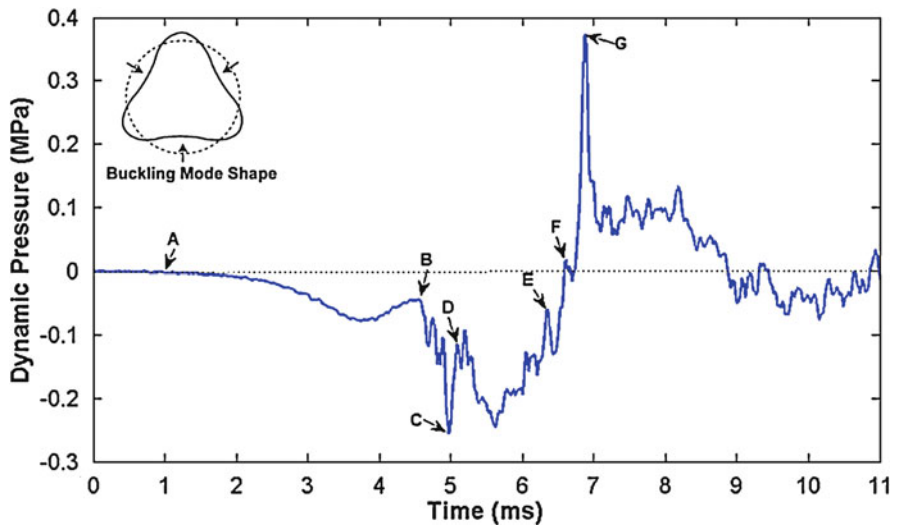


Fig. 14 Local pressure history and buckling mode shape about midspan of CT specimens

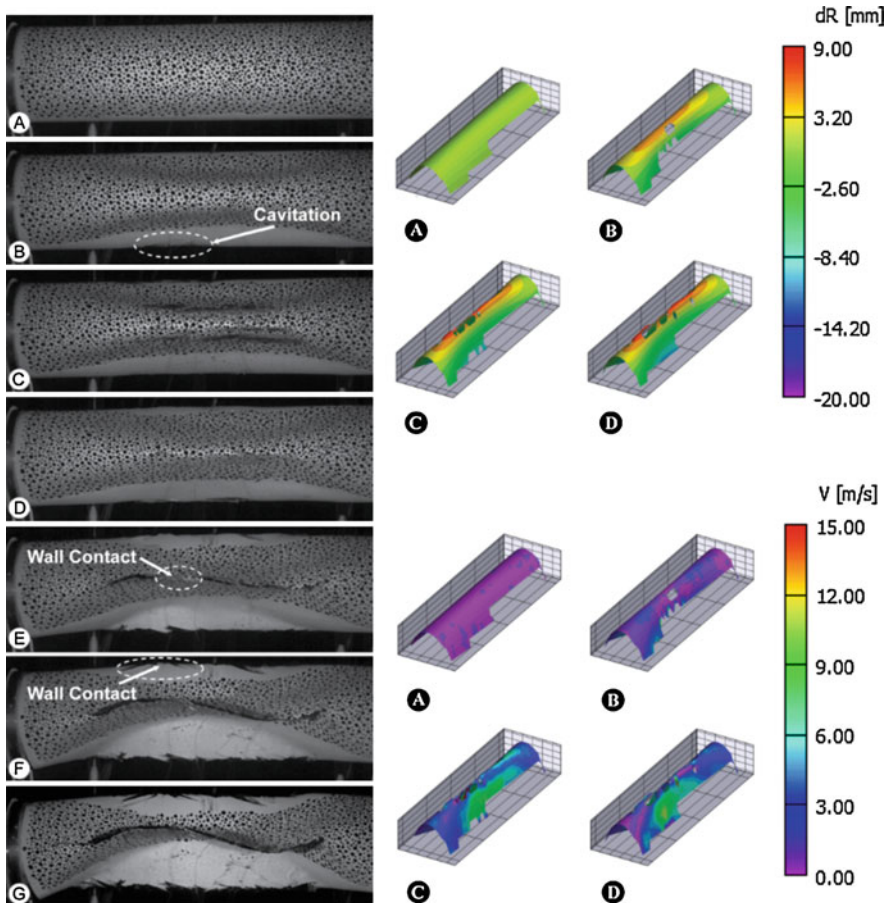


Fig. 15 High-speed photographs (left) and DIC contours of radial displacement (top-right) and velocity (bottom-right) for CT specimens

in velocity magnitude is also seen at time C, increasing from  $\sim 4$  m/s at time B to  $\sim 10$  m/s over a period of 0.5 ms, demonstrating the sudden loss of stability brought on by longitudinal cracking. Following the minimum pressure, a sudden spike in pressure is seen at time D. This spike is relatively large,  $\sim 0.15$  MPa, and has not been observed in previous implosion studies on homogeneous materials. The cause of this peak can be found by comparing images at C and D. In image C, as previously discussed, the bubbles formed by surface cavitation are at their maximum size. In image D, all visible bubbles have vanished. Between these two images, the surface cavitation bubbles collapse inward upon themselves and the surface on which they reside. The collapse of such bubbles has been well documented as resulting in large pressure pulses [41] and is, therefore, the cause of the observed spike at time D in the local pressure trace. Near the end of the under-pressure region of the pressure history, two small yet distinct peaks can be seen at times E and F. These peaks are analogous to those seen in the implosion of aluminum tubes [14, 42] and are indicative of wall-to-wall contacts at the center of the structure. After the walls contact, the collapse of the structure is abruptly halted. This causes the surrounding fluid, which accelerated inward with the surface of the structure, to rapidly decelerate. This drastic change in momentum causes the release of a high magnitude pressure pulse, observed in the pressure history at time G. Following this pulse is a broad region of overpressure as the buckling propagates through the length of the tube. Here it is seen that the tube has closed completely in the circumferential direction assuming a mode 3 buckling shape. After this point, longitudinal buckling waves develop from the applied axial compression imparted by hydrostatic pressure in conjunction with the loss in structural integrity from accumulated damage.

#### (b) Reduced Diameter Filament-Wound Specimens (CTRD)

The smaller diameter filament-wound CTRD specimens collapsed at 1.60 MPa. Interestingly, both of these specimens appeared to initiate a mode 3 collapse shape, then reduce to a mode 2 shape as the implosion progresses and the tube flattens. As with the larger specimens, the tubes return to a roughly cylindrical shape following depressurization. CTRD specimens also experience some initial quasi-static deformation, though it is significantly less than CT specimen, amounting to only  $-1.02$  mm (3% of tube radius). The reason for this difference is the increased structural rigidity of these specimens brought on by reduced diameter and increased thickness-to-radius ratio. The collapse and resulting local pressure history for CTRD specimens are quite similar to that of the larger diameter filament-wound tubes previously discussed.

#### (c) Roll-Wrapped Specimens (RC)

The RC specimens collapsed in a mode 3 buckling shape at 0.75 MPa. RC tubes experience quasi-static ovaling of  $-2.61$  mm (7% of tube radius) prior to the dynamic implosion event. This is significantly less than seen in filament-wound tubes of the same diameter, mainly due to the enhanced directional stiffness of these specimens as significantly more fibers are oriented along the major axes of the tube.

The collapse of these tubes shows many similarities to the filament-wound specimens discussed previously.

#### (d) Braided Specimens (BC)

In both tests of BC tubes, the specimens fail very rapidly at 1.81 MPa, and in both cases the collapse is so violent that the tube tears free of the sealing end caps and falls from the support structure. In these cases, the collapse mode is an imperfect mode 2 shape, with one wall drawn in toward the other, analogous to an indentation. Braided specimens show the least quasi-static ovaling of all 76.2 mm diameter specimens, amounting to  $-1.39$  mm (2.6% of tube radius). This shows that braided tubes give the least “warning” before undergoing catastrophic failure. This is a result of the deformation behavior characteristic of braided composite tubes. When braided tubes are loaded in tension, interlaced fiber tows attempt to “scissor” and straighten out. The tows then reach a point where the matrix material prohibits scissoring, causing them to “lock-up” and result in significant stiffening and ultimately brittle and catastrophic failure [43].

### 3.2.2 Hydrostatic Implosion of Thin Cylindrical Glass Fiber Composite Shells

This section further expands on the knowledge of composite shell implosion by presenting a study on the implosion of thin cylindrical glass-fiber reinforced polymer (GFRP) shells [44]. Among different composite systems, GFRPs are of particular interest to the naval industry due to their low cost and excellent resistance to both corrosion and water absorption. Specimens of varying geometry and reinforcement architecture are studied to examine the effects of these parameters on the damage and failure progression of the structure as well as the emitted pressure pulse. Two different material systems were studied, filament-wound glass fiber/polyester (PE) and braided glass fiber/epoxy. Filament-wound glass/PE tubes consist of three unidirectional glass fiber reinforcement plies arranged in an  $[\pm 55/90]$  orientation. The material properties of the specimens studied are listed in Table 6. The dimensions were selected to provide specimens with a low expected collapse pressure, and a high radius-to-thickness ratio ( $>14$ ) so that thin-wall assumptions may be utilized.

**Table 6** Geometric and material properties of studied specimens and summary of experimental results

Specimen	Reinforcement	Inner diameter (mm)	Wall thickness (mm)	L/D	Effective modulus (GPa)	$P_{cr}$ (MPa)
RT	Filament-wound	57.2	2.08	6.4	35.4	2.05[ $\pm 0.01$ ]
GT	Filament-wound	101.8	1.91	3.7	20.2	0.68[ $\pm 0.03$ ]
BG	Braided	60.1	2.03	6.3	14.7	1.94[ $\pm 0.08$ ]

Filament-wound tubes are shown to release a significantly less damaging shockwave than similar braided tubes, as more energy intensive damage mechanisms dominate the failure process. Differences in the dominating failure mechanisms present in each material produce significant differences in the pressure pulse released. Some key results are discussed below.

### 3.2.2.1 Deformation and Post-buckling Analysis

The deformation and post-buckling response of the different specimens are compared and contrasted below. For the sake of brevity, only the first case will be examined in detail and the other cases will be discussed highlighting the differences to previous cases.

#### (a) 57.2 mm Filament-Wound Tube (RT)

The smaller diameter filament-wound specimens fail at 2.05 MPa in a mode 2 buckling shape, forming two lobes. The tubes flattened completely during the dynamic failure event but were seen to rebound to a nearly cylindrical shape following the release of pressure. The local dynamic pressure history measured about the midspan of these specimens is seen in Fig. 16. High-speed photographs corresponding to marked events on that trace are included in Fig. 17.

Qualitatively, the pressure trace obtained at first appears very much like those measured for aluminum tubes by previous researchers [14, 41, 45], with a gradual decay in pressure followed by a pressure spike and a broad overpressure region. Prior to the dynamic collapse event, these specimens begin to oval significantly in a

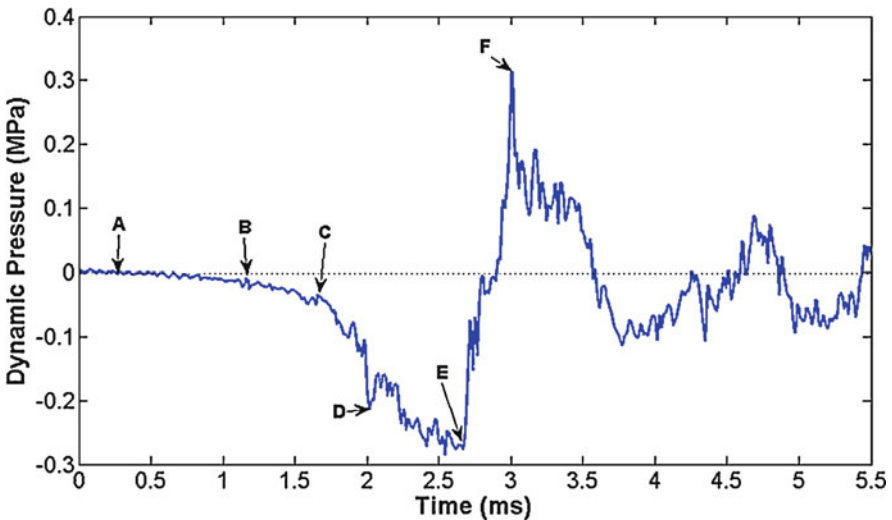
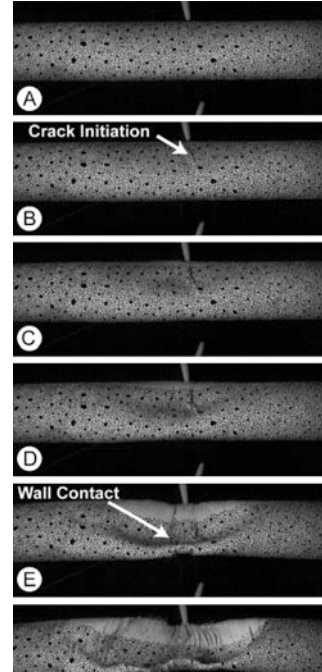


**Fig. 16** Average dynamic pressure measure about the midspan of RT specimens

**Fig. 17** High-speed photographs of key events for RT specimens



quasi-static manner. The DIC displacement data recorded a maximum radial deflection of  $-3.9$  mm (13.6% of specimen radius) at time A, indicating that this initial slow ovaling is quite significant for these tubes and this continues until time B when an unstable collapse appears to initiate. Examining the corresponding high-speed photograph, it is observed that damage also initiates at this time as indicated by the white arrow. This damage comes in the form of inter-fibrillar cracking/debonding, which will come to dominate the damage behavior of these materials. Pressure decays steadily until time C when the collapse intensifies and the matched image in Fig. 17 shows the appearance of a mode 2 dimple near the initiation of collapse. Recorded DIC data revealed that the area outside the dimple is largely unchanged from previous key point suggesting that initially, the instability is highly local.

The new rate of pressure decay is maintained fairly constant until time D where the pressure is seen to drop quite suddenly. The photograph at this time shows that the dimple formed previously has grown significantly, and that additional fiber/matrix debonding is apparent on the specimen surface. This accumulated damage effectively reduces the stiffness and structural integrity of the tube, allowing for more rapid deformation and as a result, steeper pressure drops. After this time, pressure continues to decay until a minimum value is reached. Shortly thereafter, a distinct, fairly small peak is observed at time E as pressure steeply rises. This peak is

consistent with observations on the implosion of aluminum tubes [14, 42, 45] and represents initial contact of the walls of the structure. This is confirmed using high-speed photography, as the tube is seen to make wall contact at that time in the location indicated by the white arrow. Pressure continues to rise until a maximum is reached at time F. The image at this time shows the propagation of the wall contacts both circumferentially as well as axially. This peak is followed by a broad overpressure region as the collapse continues to propagate through the length of the specimen, after which the pressure returns to oscillate about the hydrostatic value.

(b) 101.8 mm Filament-Wound Tube (GT)

The larger diameter filament-wound specimens fail at 0.68 MPa in a mode 2 buckling shape. As with the smaller specimens, these tubes regain much of their initial circularity following the collapse, and also recover significant structural stability. As is the case with the smaller RT tubes, the larger diameter GT specimens experience a significant amount of gradual ovaling prior to dynamic collapse. DIC data recorded a maximum radial deflection of  $-4.1$  mm (8.1% of specimen radius) at the start of the collapse process, similar in magnitude to that seen in the smaller specimens. Overall, the extent of damage in these specimens is remarkably less than for the smaller diameter RT specimens of the same make. This is due to the larger size of the GT specimens, coupled with a much lower collapse pressure. Therefore, the potential hydrostatic energy at collapse may be dissipated in the deformation of the structure without resulting in catastrophic damage.

(c) Braided Tube (BG)

Braided glass specimens fail at 1.94 MPa in a mode 2 buckling shape, flattening to a similar degree as aluminum specimens [14, 42, 45]. Like other specimens, circularity and structural integrity are regained following the release of pressure though to an even larger degree. The average local pressure history measured about the midspan of a typical specimen is seen in Fig. 18. The pressure trace for these specimens appears quite different from filament-wound glass/PE tubes discussed previously. Because dimensions and collapse pressures are very similar, this can be attributed to the change in reinforcement architecture. An amount of initial ovaling did occur in these specimens, although it is considerably less than either filament-wound specimen. DIC records a maximum deflection of  $-1.3$  mm (4.3% of specimen radius) at time A. The dynamic collapse begins with a relatively slow decay in pressure from time A to time B, lasting  $\sim 2.25$  ms. This is much longer than the initial gradual decay seen in RT tubes, which lasted  $\sim 1$  ms before intensifying. At time B, a slight recovery in pressure is seen followed by a very sharp drop to a minimum at time C which indicates initiation of major longitudinal cracking. The under-pressure region continues until time E where a distinct peak is observed followed by a rapid increase in pressure, indicating wall contact. After wall contact is made the high magnitude pressure pulse typical of the implosion arrives at time F.

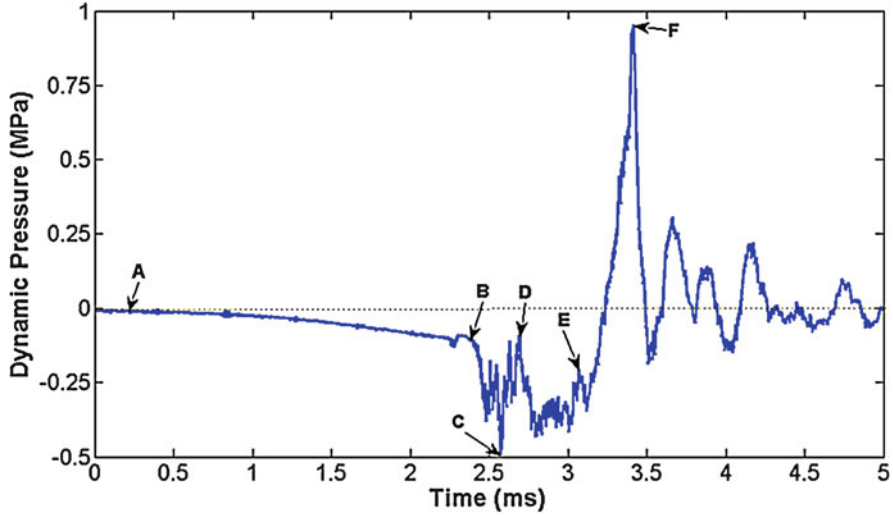


Fig. 18 Average dynamic pressure measure about the midspan of BG specimens

### 3.2.3 Shock-Initiated Buckling of Carbon/Epoxy Composite Tubes at Sub-Critical Pressures

An implosion caused by quasi-static pressurization to this critical pressure is known as a natural implosion. However, implosions can also be initiated at sub-critical pressures with an underwater explosive (UNDEX) loading. If a structure experiences a high magnitude shock –wave loading such as that generated by a near-field UNDEX, it may collapse at a relatively low hydrostatic pressure [46]. The study discussed here [47] focuses on this extreme condition for composite materials. The implodable volumes in this study were carbon/epoxy filament wound composite tubes, consisting of seven layers of unidirectional carbon fabric reinforcement arranged in a  $[\pm 15/0/\pm 45/\pm 15]$  layup with a 60.3 mm inner diameter and 381 mm unsupported length with a nominal wall thickness of 1.63 mm. The dimensions are selected to provide specimens with a relatively low expected collapse pressure. The critical natural collapse pressure of these tubes was found to be 0.90 MPa. To generate the explosive load, an exploding-bridgewire detonator of 80 mg PETN and 1031 mg RDX (RP-85, Teledyne RISI, Inc., Tracy, CA) is mounted directly behind the specimen at a controlled standoff distance of either 102 mm (near-field), 203 mm (mid-field) or 305 mm (far-field).

The model proposed by Shin [48] is fitted to recorded peak pressure data at several standoff distances, to obtain a relationship by which the peak pressure could be predicted as a function of any standoff distance. The fit model was used to determine maximum incident pressures listed in Table 7 for the afore-mentioned standoff distances.



**Table 7** Summary of explosive-initiated implosion experiments

Case	Hydrostatic pressure (MPa)	Explosive standoff (mm)	Peak predicted incident pressure (MPa)	Time before implosion (ms)
1	0.71	102	45.9	0.93
2	0.71	203	20.2	6.83
3	0.71	305	12.4	15.22

When a sealed composite tube is subjected to explosive loading, the pressure waves that travel through the walls of the structure are not solely compressive. If this tube is filled with a low impedance material such as air, tensile waves of significant magnitude will be caused in the tube wall by the impedance mismatch at the interior interface. This tensile loading has the potential to degrade the stability of the structure, as it may cause damage in the matrix material or at the fiber-matrix interface which is highly sensitive to out-of-plane tension [49]. When an underwater explosive is detonated, the decomposed gases of the charge create an expanding superheated gas bubble. After reaching its maximum critical size, the surrounding hydrostatic pressure of water causes the bubble to collapse, and upon completion of this collapse, a relatively strong and fairly broad pressure pulse known as the “bubble pulse” is emitted [50]. The magnitude of the bubble pulse is typically much smaller than that of the initial shock wave, however, due to its long duration, the impulse is of comparable strength and it interacts with the deforming shell to potentially cause its implosion. Based on the stand-off distance, the following behaviors were noted:

(a) Near-Field Explosion

In this case, the tube implodes in mode 2 shortly after experiencing the initial shock from the explosive. The average local pressure history measured about the midspan of a typical specimen is seen in Fig. 19. The initiation of the instability occurs at approximately 0.93 ms, well before the arrival of reflections from the tank wall, so it may be concluded that the initial shock wave alone possesses sufficient energy to trigger the collapse at this sub-critical static pressure. Wall contact occurs 5.00 ms after the initiation of the implosion, roughly consistent with results from natural implosion experiments. This implies that though the initiation mechanism of the collapse is different, the subsequent mechanics of the collapse are the same as for a natural implosion. In this case, no implosion pulse is detectable in the pressure history following wall contact due to the noisy nature of the pressure signal at this time caused by the superposition of reflections of the initial shock and bubble pulses from the tank walls.

(b) Mid-Field Explosion

Implosion in mode 2 again occurs in this case, though it is much later in the time than the 102 mm standoff case, initiating 6.83 ms after the detonation of the charge. This delayed collapse shows that neither the initial shock wave nor the reflections of that



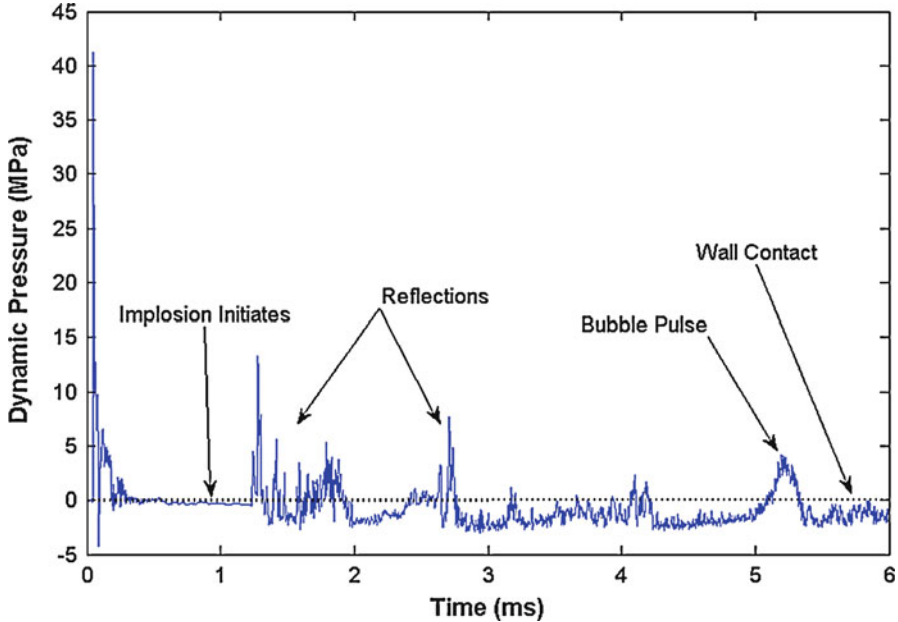


Fig. 19 Pressure history for explosive experiments with 102 mm (near-field) standoff distance

shock from the tank walls are sufficient to cause the collapse at this charge distance. The instability is triggered after the first bubble pulse showing that for this standoff distance, the bubble pulse is the cause of the implosion. The tube continues to collapse until wall contact is made 2.43 ms after initiation, which is significantly shorter than the collapse time of the natural implosion (4.7 ms). The reason behind this reduction in collapse time, as well as the reason for the timing of the collapse, is related to the wave interaction discussed in the reference publication by Pinto and Shukla [47].

### (c) Far-field Explosion

Similar to the previous two cases, these tubes implode in a mode 2 shape, however, they collapse very late in the event, initiating 15.22 ms after the detonation of the charge. This is long after both the initial shock and the first bubble pulse, showing that neither of these events triggers the collapse on their own. Wall contact occurs at 1.83 ms following the initiation of the implosion, even shorter than for the 203 mm standoff case. Like the 203 mm standoff case, the cause for the delayed collapse as well as the duration of the collapse is due to the accumulation of damage caused by each successive loading event from the bubble pulses. This damage continually degrades the structural stiffness, until the vibrations caused by the impulse coupled with hydrostatic pressure can drive the implosion.

### 3.3 Mitigation of Pressure Pulses from Implosion of Thin Composite Shells

This section details a recent work done on mitigation of dangerous pressure released from the implosion of composite shells by addition of polymeric layers [51]. It was seen in Sect. 2.4 that polyurea (PU) coatings can serve as a useful addition to mitigate the blast response of composite materials. Layers of controlled thicknesses were applied to carbon/epoxy tubes on both the interior and exterior of the tube to determine the effect of coating thickness on the composite structure.

The implodable volumes used in this study were the same geometry and material as the ones used in Sect. 2.2.3.

Specimens were coated with a two-part PU which has a low stiffness (~10 MPa), but very high elongation of approximately 500%. For this reason, polyurea is very attractive for energy absorption applications. A simple fixture was built to coat both exterior and interior of the composite tubes with a controlled thickness of the mixed polymer. In this study, two coating thicknesses were used: a “thin” coating having equal volume to the tube walls, and a “thick” coating, with double the thickness of the “thin” coating. It should be noted that the interior and exterior coatings have slightly different thicknesses due to their locations on the tube, but their volumes, and therefore masses, are approximately the same (as shown in Table 8). Results show that thick interior coatings significantly reduce the energy released in the pressure pulse, at the cost of an increase in the overall mass of the structure. Surprisingly, thick exterior coatings increase the energy released, thus making the collapse more dangerous. These findings provide useful guidelines in the design of marine composite structures susceptible to implosion. The flow energy obtained directly as a function of pressure, is a useful tool for comparing the total energy emitted during the implosion process. By making an assumption of spherical symmetry of the emitted pressure pulse, the energy flux through a surface at distance,  $R$ , up to an arbitrary time,  $t$ , is defined simply as [52]:

$$E_F = \frac{1}{2\rho_0 R_s} \left[ \int_0^t \Delta p dt \right]^2 \quad (9)$$

**Table 8** Summary of experimental results

Specimen	Collapse pressure, $P_{cr}$ (MPa)	$P_{min}/P_{cr}$	$P_{max}/P_{cr}$	Maximum collapse velocity (m/s)	Pre-buckling displacement (mm)
Aluminum	1.68 [ $\pm 0.01$ ]	0.69 [ $\pm 0.04$ ]	1.70 [ $\pm 0.17$ ]	20.0 [ $\pm 2.0$ ]	2.5 [ $\pm 0.2$ ]
Carbon/epoxy	0.97 [ $\pm 0.03$ ]	0.51 [ $\pm 0.05$ ]	2.57 [ $\pm 0.56$ ]	16.5 [ $\pm 2.3$ ]	1.7 [ $\pm 0.5$ ]
Glass/PE	2.05 [ $\pm 0.01$ ]	0.84 [ $\pm 0.02$ ]	1.24 [ $\pm 0.06$ ]	27.2 [ $\pm 1.4$ ]	3.9 [ $\pm 0.2$ ]

where  $\Delta p$  is the dynamic pressure at time  $t$ ,  $R_s$  is the standoff distance, and  $\rho_0$  is the density of the fluid. To find the total flow energy, a spherical wave is assumed and the flux is multiplied by the area of an imaginary sphere with radius equal to the standoff distance of the pressure sensor as follows:

$$E_A = 4\pi R_s^2 E_F \quad (10)$$

To normalize this measure for differences in the collapse pressure of different materials, the total flow energy is divided by the potential hydrostatic energy available just prior to the collapse, defined as:

$$E_H = P_{cr} V_{tube} \quad (11)$$

where  $P_{cr}$  is the hydrostatic collapse pressure and  $V_{tube}$  is the internal volume of the tube. In this way, the flow energy released in the pressure pulse may be presented as a percentage of the available hydrostatic energy at the collapse pressure. Due to the knowledge of the shape of the pulse, the signal of a single sensor may be used to calculate the flow energy as described above. Some of the results are discussed below:

(a) Over-pressure comparison

For exterior coatings, thin coatings have little effect on the peak pressure, while thick coatings produce a significantly higher magnitude pressure peak. The maximum pressure for the thick exterior coated case is approximately 80% greater than the uncoated case which gives more evidence that thick exterior coatings actually intensify the collapse of the structure. This appears to be due to a containment of the damage in the structure and is discussed further in later sections.

The interior coatings show even more interesting changes to the overpressure. Not only is the magnitude of the pressure pulse altered, but so is the timing of the pulse. As the thickness of the coating increases, the magnitude of the pressure pulse decreases, and the arrival of the pulse is delayed. The mitigation of the peak pressure again gives evidence that these coatings slow the collapse of these tubes, thereby lessening the severity of the pressure pulse. The change in timing of the peak suggests these coatings extend the contact event itself, meaning that it takes longer to arrest the structure and the deceleration of the tube walls is therefore less.

(b) Flow energy

The flow energy as a percentage of the total available hydrostatic potential energy is dependent on the different material cases. Starting with thin coatings, it is seen that both interior and exterior coatings show little effect on the flow energy developed. Though there is some change in mean value, any change from the control uncoated case lies within error bars. Coatings of this thickness had little effect on the severity of the collapse. Thick coatings, on the other hand, do have a significant effect on the flow energy released. Thick interior coatings show a significant (30%) reduction in

flow energy developed in the collapse. This implies that this coating drastically reduces the severity of the collapse, and this is supported by the analyses previously discussed. Tubes with thick interior coatings showed less of a pressure drop, reduced collapse velocity, and lower peak acceleration. All of these factors contribute to lessening the intensity of the failure event, and in turn reducing the flow energy released. Conversely, thick exterior coatings show a significant (14%) increase in flow energy, however, much higher peak pressure is observed for these cases.

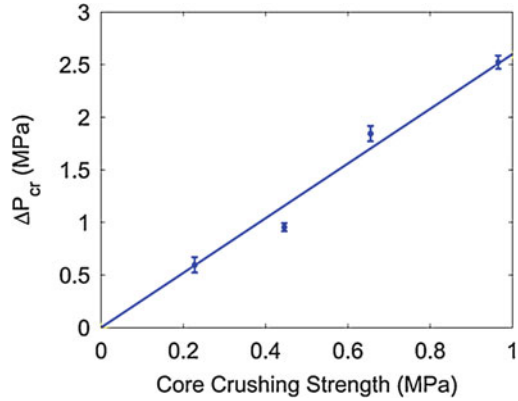
### ***3.4 Hydrostatic and Shock-Initiated Instabilities in Double-Hull Composite Cylinders***

This section presents a study on the stability and dynamic behavior of concentric composite cylinders, with and without foam cores, during underwater an implosion [53]. Both hydrostatic and shock-initiated implosions of these double-hull cylinders are considered. These structures provide increased stability through bending strength, as well as pulse mitigation through foam core crushing. The specimens used in this study consist of commercially available filament wound sanded carbon/epoxy carbon fiber cylinders placed concentrically and bonded with PVC foam cores filling up the gap. Both the inner and outer shells have a filament winding architecture of  $[\pm 15^\circ/+87^\circ/\pm 45^\circ/\pm 15^\circ]$ . The outer shell has a 60.3 mm ID and the inner shell a 38.1 mm ID, with both shells having a 279.4 mm unsupported length. The measured average wall thicknesses of the outer and inner shells used in this study are 1.69 mm and 1.68 mm, respectively. The closed cell PVC foam cores used in the specimens are cut from Divinycell H series foam-sheets provided by DIAB, Inc. (DeSoto, TX). Cores are made by cutting rings of 41.2 mm ID and 9.6 mm radial thickness. Rings are then stacked concentrically between the inner and outer shells. Foam cores of different densities are used: experiments are performed with no foam core, Divinycell H35, H60, H80, and H100. Results show a substantial increase in structural stability when the foam core is added, with critical collapse pressure increasing linearly with core crushing strength under hydrostatic conditions, and collapse delayed substantially or prevented under dynamic pulse loading.

#### **3.4.1 Collapse Pressure**

It is important to be able to predict the buckling behavior of a double hull structure as a function of material and geometrical properties. Figure 20 shows that the  $\Delta P_{cr}$  values (defined as the increase in collapse pressure of the outer shell due to the sandwich structure [54]) measured previously increase linearly with core crushing strength, intersecting the origin and having a non-dimensional slope of 2.6. This implies that for the given core geometry, it would be possible to find a higher

**Fig. 20** Increase in collapse pressure as a function of foam core crushing strength



strength material than those studied here and that using such a core would likely increase buckling strength along the line in Fig. 20.

### 3.4.2 Implosion Under Hydrostatic Pressure: Observed Collapse Behaviors

Three overarching behaviors were observed in the collapse of the double hull specimens. In the first case, the outer cylinder collapsed and crushed the foam core but the inner cylinder did not collapse. In the second case, the outer cylinder collapsed and crushed the foam core, after which there was a brief dwell time before the inner cylinder collapsed. The last case shows that the outer cylinder collapsed, crushed the foam core, and collapsed the inner cylinder in a singular motion, with no dwell in between. Only the one case of collapse with dwell is discussed for illustration.

#### 3.4.2.1 Complete Collapse With Dwell

Figure 21 shows the pressure pulse recorded in cases where the outer cylinder collapses, a brief dwell occurs, and then the inner cylinder collapses. Here, buckling initiation of the outer cylinder occurs at (A), followed by a smooth under-pressure region that exists until the onset of matrix cracking and the associated drop in fluid pressure at (B). The under-pressure region then continues until (C), where the pressure trace crosses the zero dynamic pressure line and an initial over-pressure corresponding to the collapse of the outer cylinder against the inner cylinder is recorded at (D). Following that, the inner cylinder begins to buckle from the hydrostatic pressure. What follows is a secondary implosion pulse corresponding to the collapse of the inner cylinder, with a new under-pressure region in the pressure signal being created at (E). At (F), there is a spike in pressure which corresponds to the development of damage in the inner cylinder as it collapses. The under-pressure

**Fig. 21** Normalized pressure pulses from cases where the outer cylinder collapsed, dwelled briefly, then the inner cylinder collapsed; H100 foam core case, measured at midsection; outer cylinder buckling mode shape and sensor location

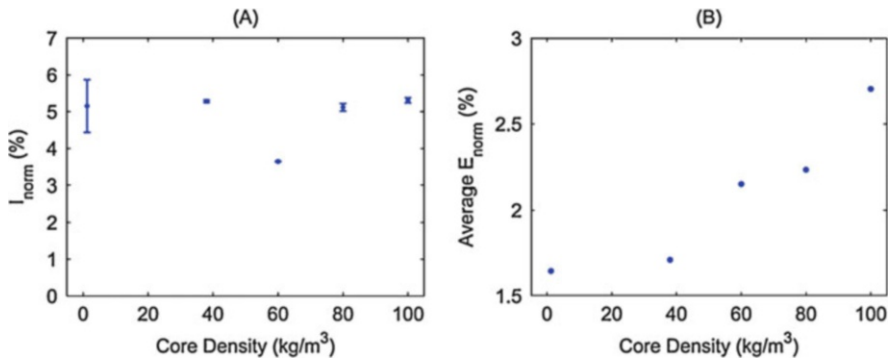
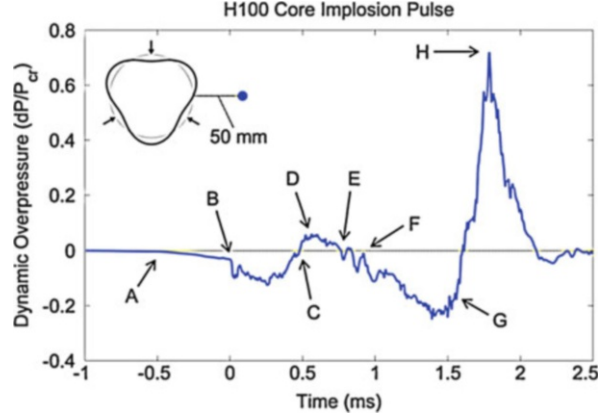


**Fig. 22** Implosion emissions as a function of core density showing (A) normalized under-pressure impulse; (B) normalized average waveform energy

region continues until (G), where the inner cylinder makes wall contact with itself, and a secondary pressure peak at H is created which exceeds that of the first in amplitude.

### 3.4.3 Implosion Under Hydrostatic Pressure: Impulse and Energy

It is useful to look at normalized impulse,  $I_{norm}$ , defined as the area of the under-pressure region in the dynamic pressure versus time plot normalized by the product of collapse pressure and total under-pressure duration. It is plotted for various implosion cases in Fig. 22A with foam core density on the horizontal axis. The almost constant value of the impulse with foam core density implies that the impulse is mainly a function of collapse pressure, and is not directly influenced by core density or other properties. A plot of normalized average energy values ( $E_{norm} = E_A/E_H$ ) which present the energy emitted by the implosion event as a function of available hydrostatic energy, is given in Fig. 22B.

The exception to this trend in the data is the case of the H60 core, which has a lower magnitude normalized impulse because of the uniquely long time delay between the collapse of the inner and outer cylinder. There, normalized average energy released increases with core density. The experiments showed a more violent collapse phenomenon with the H60, -80, and -100 cases. These experiments also showed increased variation in energy released because the inner cylinder also collapses in the aforementioned cases, and introduces new damage mechanisms. The increase in normalized energy with core density is also significant, as there is a 57% increase in average normalized energy released between H35 and H100 core specimens. This highlights the diminishing returns on energy absorption for higher density cores. Increasing core density increases both hydrostatic collapse pressure and the energy released from the implosion. However, the increase in energy released from implosion is greater than the increase in potential energy from collapse pressure ( $dE_A/dE_H > 0$ ) as core density increases. Thus, increasing core density is not an effective means of mitigating energy release from the natural implosion of double hull composite cylinders.

#### **3.4.4 Implosion Under Combined Hydrostatic and Shock Initiated Loadings: Pressure History**

For shock-initiated implosion experiments, an exploding-bridgewire detonator of 80 mg PETN and 1031 mg RDX (RP-85, Teledyne RISI, Inc., Tracy, CA) is mounted directly behind the specimen at a controlled standoff distance of either 102 mm or 203 mm. After filling, the vessel is pressurized to 80% of the measured natural buckling pressure of the specimen and the charge is detonated causing the specimen to experience shock loading. The superposition of the explosive pulse on top of the hydrostatic pressure causes complex loading on the underwater structure. The structures without foam cores collapsed completely in all experiments. Specimens collapsed in the same stages, regardless of whether they were subject to 102 mm or 203 mm explosive standoff. There, collapse initiation of the outer cylinder is seen, followed by outer-inner cylinder impact. After that, there is a period of time wherein the two cylinders vibrate and deform inward radially before the collapse of the inner cylinder begins with inner-inner wall contact occurring. Following this, the collapsed area propagates along the length of the structure, until it reaches the final collapse state. The specimens with foam core either implode quickly or undergo long-term vibrations. In the latter case, specimens may either survive completely, or implode after an extended period of time as a result of damage development during vibration. These vibrations provide an additional mechanism of energy absorption. The time period of vibration of the cylinders is influenced by both the added mass of water and the initial hydrostatic pressure [13].

**Acknowledgments** The authors acknowledge the financial support provided by Dr. Yapa D.S. Rajapakse, Solid Mechanics Program Manager ONR under grant numbers N00014-01-1-1033, N00014-04-1-0248, N00014-10-1-0662, and N00014-15-1-2046. The authors also

acknowledge the support provided by the Department of Homeland Security (DHS) under Cooperative Agreement No. 2008-ST-061-ED0002. The authors would like to thank TPI Composites for providing the facilities used to create some of the composite structures discussed in this chapter. Finally, the help of graduate and undergraduate students working in the Dynamic Photo Mechanics Lab during this period is gratefully acknowledged.

## References

1. Perl R, O'Rourke R (2001) Terrorist attack on USS Cole: background and issues for congress. Emerging technologies: recommendations for counter-terrorism. Institute for Security Technology Studies, Dartmouth College
2. Perl R (1998) Terrorism: US responses to bombings in Kenya and Tanzania: a new policy direction? Congressional report. Congressional Research Service, The Library of Congress
3. Thomas GP (2013) Composites in combat: composites for military vehicles. AZO Materials. <https://www.azom.com/article.aspx?ArticleID=8166>. Accessed 12 Oct 2018
4. Mouritz AP, Gellert E, Burchill P, Challis K (2001) Review of advanced composite structures for naval ships and submarines. *Compos Struct* 53(1):21–42
5. Xue Z, Hutchinson JW (2003) Preliminary assessment of sandwich plates subject to blast loads. *Int J Mech Sci* 45(4):687–705
6. Fleck NA, Deshpande VS (2004) The resistance of clamped sandwich beams to shock loading. *J Appl Mech* 71(3):386–401
7. Dharmasena KP, Wadley HNG, Xue Z, Hutchinson JW (2008) Mechanical response of metallic honeycomb sandwich panel structures to high-intensity dynamic loading. *Int J Impact Eng* 35(9):1063–1074
8. Yi J, Boyce MC, Lee GF, Balizer E (2005) Large deformation rate-dependent stress-strain behavior of polyurea and polyurethanes. *Polymer* 47(1):319–329
9. Amirkhizi AV, Isaacs J, McGee J, Nemat-Nasser S (2006) An experimentally-based constitutive model for polyurea, including pressure and temperature effects. *Philos Mag* 86(36):5847–5866
10. Hoo Fatt MS, Ouyang X, Dinan RJ (2004) Blast response of walls retrofitted with elastomer coatings. *Struct Mater* 15:129–138
11. Roland CM, Twigg JN, Vu Y, Mott PH (2006) High strain rate mechanical behavior of polyurea. *Polymer* 48(2):574–578
12. Tekalur SA, Shukla A, Shivakumar K (2008) Blast resistance of polyurea based layered composite materials. *Compos Struct* 84(3):271–281
13. Gupta S, Matos H, LeBlanc J, Shukla A (2016) Shock initiated instabilities in underwater cylindrical structures. *J Mech Phys Solids* 95:188–212
14. Turner SE, Ambrico JM (2012) Underwater implosion of cylindrical metal tubes. *J Appl Mech* 80(1):1–11
15. Gupta S, LeBlanc J, Shukla A (2015) Sympathetic underwater implosion in a confining environment. *Extreme Mech Lett* 3:123–129
16. von Mises R (1914) The critical external pressure of cylindrical tubes *Zeitschrift des Vereines Dtsch. Ingenieurs* 58(19):750–767
17. von Mises R (1929) The critical external pressure of cylindrical tubes under uniform radial and axial load. *Stodola's Festschrift, Zurich*, pp 418–430
18. Cartlidge E (2001) Accident grounds neutrino lab. IOP Publishing Physicsworld. <https://physicsworld.com/a/accident-gro>
19. Kumar P, LeBlanc J, Stargel D, Shukla A (2012) Effect of plate curvature on blast response of aluminum panels. *Int J Impact Eng* 46:74–85



20. LeBlanc J, Shukla A, Rousseau C, Bogdanovich A (2007) Shock loading of three-dimensional woven composite materials. *Compos Struct* 79(3):344–355
21. Wright J (1961) Shock tubes. Wiley, New York
22. Xue Z, Hutchinson JW (2004) A comparative study of impulse-resistant metal sandwich plates. *Int J Impact Eng* 30(10):1283–1305
23. Taylor GI (1963) Pressure and impulse of submarine explosion waves on plates. In: Batchelor GK (ed) *The scientific papers of Sir Geoffrey Ingram Taylor, aerodynamics and the mechanics of projectiles and explosions*, vol 2. Cambridge university press, Cambridge, pp 287–303
24. Kambouychev N (2007) Ph. D dissertation, Massachusetts Institute of Technology
25. Kambouychev N, Noels L, Radovitzky R (2006) Nonlinear compressibility effects in fluid-structure interaction and their implications on the air-blast loading of structures. *J Appl Phys* 100:063519
26. Wang E, Jefferson W, Shukla A (2011) Analytical and experimental study on the fluid structure interaction during air blast loading. *J Appl Phys* 110:114901
27. Baker WE, Cox PA, Westine PS, Kulesz JJ, Strehlow RA (1983) *Explosion hazards and evaluation*. Elsevier Publishing Company, New York
28. Glasstone S, Dolan PJ (1964) *The effects of nuclear weapons*. Third edition. United States, p 1977. <https://doi.org/10.2172/6852629>
29. Smith PD, Hetherington JG (1994) *Blast and ballistic loading of structures*. Butterworth-Heinmann, Elsevier Science Ltd, Oxford
30. Wang E, Gardner N, Gupta S, Shukla A (2012) Fluid-structure interaction and its effect on the performance of composite structures under air-blast loading. *Int J Multiphys* 6(3):219–239
31. Li R, Kardomateas GA, Simitse GJ (2009) Point-wise impulse (blast) response of a composite sandwich plate including core compressibility effects. *Int J Solids Struct* 46(10):2216–2223
32. Gardner N, Wang E, Shukla A (2012) Performance of functionally graded sandwich composite beams under shock wave loading. *Compos Struct* 94(5):1755–1770
33. <http://www.gurit.com>
34. Gardner N (2012) *Novel composite materials and sandwich structures for blast mitigation*. Ph. D dissertation, University of Rhode Island
35. Wang E, Gardner N, Shukla A (2009) The blast resistance of sandwich composites with stepwise graded cores. *Int J Solids Struct* 46(18–19):3492–3502
36. Gardner N, Kumar P, Wang E, Shukla A (2012) Blast mitigation in a sandwich composite using graded core and polyurea interlayer. *Exp Mech* 52(2):119–133
37. <http://specialty-products.com>
38. Schreier H, Orteu JJ, Sutton MA (2009) *Image correlation for shape, motion and deformation measurements: basic concepts, theory and applications*. Springer, New York
39. Gupta S, Parameswaran V, Sutton MA, Shukla A (2014) Study of dynamic underwater implosion mechanics using digital image correlation. *Proc R Soc A Math Phys Eng Sci* 470:20140576–20140576. <https://doi.org/10.1098/rspa.2014.0576>
40. Pinto M, Gupta S, Shukla A (2015) Study of implosion of carbon/epoxy composite hollow cylinders using 3-D digital image correlation. *Compos Struct* 119:272–286. <https://doi.org/10.1016/J.COMPSTRUCT.2014.08.040>
41. Brennen CE (Christopher E) (2014) *Cavitation and bubble dynamics*. Cambridge University Press, New York
42. Ikeda CM, Wilkerling J, Duncan JH (2013) The implosion of cylindrical shell structures in a high-pressure water environment. *Proc R Soc A Math Phys Eng Sci* 469:20130443–20130443. <https://doi.org/10.1098/rspa.2013.0443>
43. Harte A-M, Fleck NA (2000) On the mechanics of braided composites in tension. *Eur J Mech A Solids* 19:259–275. [https://doi.org/10.1016/S0997-7538\(99\)00164-3](https://doi.org/10.1016/S0997-7538(99)00164-3)
44. Pinto M, Gupta S, Shukla A (2015) Hydrostatic implosion of GFRP composite tubes studied by digital image correlation. *J Press Vessel Technol* 137:051302. <https://doi.org/10.1115/1.4029657>

45. Farhat C, Wang KG, Main A et al (2013) Dynamic implosion of underwater cylindrical shells: experiments and computations. *Int J Solids Struct* 50:2943–2961. <https://doi.org/10.1016/J.IJSOLSTR.2013.05.006>
46. Lindberg HE, Florence AL (1987) *Dynamic pulse buckling*. Springer Netherlands, Dordrecht
47. Pinto M, Shukla A (2016) Shock-initiated buckling of carbon/epoxy composite tubes at sub-critical pressures. *Exp Mech* 56:583–594. <https://doi.org/10.1007/s11340-015-0033-1>
48. Shin YS (2004) Ship shock modeling and simulation for far-field underwater explosion. *Comput Struct* 82:2211–2219. <https://doi.org/10.1016/J.COMPSTRUC.2004.03.075>
49. Sridharan S (2008) *Delamination behaviour of composites*. CRC Press, Boca Raton
50. Cole RH (1948) *Underwater explosions*. Princeton University Press, Princeton
51. Pinto M, Shukla A Mitigation of pressure pulses from implosion of hollow composite cylinders. <https://doi.org/10.1177/0021998315624254>
52. Arons AB, Yennie DR (1948) Energy partition in underwater explosion phenomena. *Rev Mod Phys* 20:519–536. <https://doi.org/10.1103/RevModPhys.20.519>
53. DeNardo N, Pinto M, Shukla A (2018) Hydrostatic and shock-initiated instabilities in double-hull composite cylinders. *J Mech Phys Solids* 120:96–116. <https://doi.org/10.1016/j.jmps.2017.10.020>
54. Glasstone, S, and Dolan, P J. *The Effects of Nuclear Weapons*. Third edition. United States. 1977. <https://doi.org/10.2172/6852629>